View metadata, citation and similar papers at core.ac.uk
brought to you by CORE
provided by Helsingin yliopiston digitaalinen arkisto

Department of Chemistry
University of Helsinki
Finland

Optical and structural properties of Si nanocrystals in SiO_2 film

Timur Nikitin

ACADEMIC DISSERTATION

To be presented, with the permission of the Faculty of Science of the University of Helsinki, for public examination in lecture hall A129 of the Department of Chemistry (A. I. Virtasen aukio 1) on November 18th 2013, at 12 o'clock.

Helsinki 2013

Supervisors

Docent Leonid Khriachtchev
Professor Markku Räsänen
Laboratory of Physical Chemistry
Department of Chemistry
University of Helsinki

Reviewers

Doctor Fabrice Gourbilleau
NIMPH Team
French National Centre for Scientific Research
France

and

Professor Ivan Pelant
Institute of Physics
Academy of Sciences
Czech Republic

Opponent

Professor Lorenzo Pavesi
Nanoscience Laboratory
University of Trento
Italy

ISBN 978-9521094897 (pbk.)
ISBN 978-9521094903 (PDF)

Helsinki University Printing House
Helsinki 2013

Abstract

Silicon nanocrystals (Si-nc) embedded in a SiO_2 matrix is a promising system for silicon-based photonics. We studied optical and structural properties of Si-rich silicon oxide SiO_x ($x < 2$) films annealed in a furnace at temperatures up to 1200 °C and containing Si-nc. The measured optical properties of SiO_x films are compared with the values estimated by using the effective medium approximation and X-ray photoelectron spectroscopy (XPS) results. A good agreement is found between the measured and calculated refractive index. The results for absorption suggest high transparency of nanoscale suboxide. The extinction coefficient for elemental Si is found to be between the values for crystalline and amorphous Si. Thermal annealing increases the degree of Si crystallization; however, the Si–SiO_2 phase separation is not complete after annealing at 1200 °C. The 1.5-eV photoluminescence probably originates from small (~1 nm) oxidized Si grains or oxygen-related defects, but not from Si-nc with sizes of about 4 nm. The SiO_x films prepared by molecular beam deposition and ion implantation are structurally and optically very different after preparation but become similar after annealing at ~1100 °C. The laser-induced thermal effects found for SiO_x films on silica substrates illuminated by focused laser light should be taken into account in optical measurements.

Continuous-wave laser irradiation can produce very high temperatures in free-standing SiO_x and Si/SiO_2 superlattice films, which changes their structure and optical properties. The center of a laser-annealed area is very transparent and consists of amorphous SiO_2. Large Si-nc (up to 300 nm) are observed in the ring around the central region. These Si-nc produce high absorption and they are typically under compressive stress, which is connected with the crystallization from the melt phase. Some of the large Si-nc exhibit surface features, which is interpreted in terms of eruption of pressurized Si from the film. A part of large Si-nc is removed from the film forming holes of similar sizes. The presence of oxygen in the laser-annealing atmosphere decreases the amount of removed Si-nc. The structure of laser-annealed areas is explained by thermodiffusion, which leads to the macroscopic Si–SiO_2 phase separation. Comparison of the structure of central regions for laser annealing in oxygen, air, and inert atmospheres excludes the dominating effect of Si oxidation in the formation of laser-annealed area. By using a strongly focused laser beam, the structural changes in the free-standing films can be obtained in submicron areas, which suggests a concept of nonvolatile optical memory with high information density and superior thermal stability.

Acknowledgements

This research was carried out in the Laboratory of Physical Chemistry in the University of Helsinki during 2007–2013. FinNano Project "Optical and Surface Properties of Nanoparticles" (OPNA), the Finnish Center of Excellence "Computational Molecular Science", the University of Helsinki Research Funds (HENAKOTO), and Magnus Ehrnrooth Foundation supported this work financially.

I am grateful to Professor Markku Räsänen for giving me the opportunity to work in the Laboratory of Physical Chemistry and for providing necessary support during this research. My main supervisor, Dr. Leonid Khriachtchev, is greatly acknowledged for introducing me to the topic of silicon nanocrystals, sharing his vast scientific experience, and helpful guidance during the research.

I would like to acknowledge all co-authors of Papers I-VIII for their invaluable contribution and especially Dr. Sergei Novikov for sample preparation. Doctor Fabrice Gourbilleau and Professor Ivan Pelant are thanked for reviewing this thesis. The Head of the Laboratory of Physical Chemistry, Lauri Halonen and all other members of the Laboratory are thanked for making this place a pleasant environment to work in. Especially I would like to mention my roommate Ksenia Marushkevich, Alexandra Domanskaya, Antti Lignell, Masashi Tsuge, Qian Cao, and Susy Lopes.

I am thankful to all my friends in Finland for making the adaptation in a foreign country easy and for keeping me company outside the University.

Last but not least, I would like to warmly thank my family for their continuous support and love.

Contents

Abstract 3

Acknowledgements 4

Contents 5

List of original publications 7

1 Introduction 10

1.1 Light emission from Si nanocrystals 10

1.2 Optical and structural properties of Si-nc in silica 11

1.3 Theoretical studies of optical properties of Si-nc 13

1.4 Fabrication of Si-nc 13

1.5 Laser annealing 13

1.6 Characterization techniques used in this study 14

2 Experimental details and methods 16

2.1 Samples 16

2.1.1 Molecular beam deposition 16

2.1.2 Si-ion implantation 16

2.2 Equipment 16

2.3 Methods 17

2.3.1 PL-filtering effect 17

2.3.2 XPS spectra 20

2.3.3 Effective medium approximation 21

2.3.4. Temperature measurements 21

2.3.5 Tauc law 22

3 Results and discussions 23

3.1 Furnace-annealed SiO_x ($x < 2$) films on silica substrates 23

3.1.1 Correlation between optical and structural properties 23

3.1.2 Photoluminescence of the MBD samples 28

3.1.3 Comparison of ion implantation and MBD (x ~ 1.8) 30

3.1.4 Laser heating of films on substrates 32

3.2 Laser annealing of free-standing films 33

3.2.1 Laser-annealed areas 33

3.2.2 Surface structure 35

3.2.3 Effect of the annealing atmosphere 37

3.2.4 Effect of the exposure duration 41

3.2.5 Optical memory 43

4. Conclusions in brief 46

References 48

List of original publications

This thesis is based on the following publications, which are referred to by the Roman numerals I-VIII:

I. L. Khriachtchev, **T. Nikitin**, C. J. Oton, R. Velagapudi, J. Sainio, J. Lahtinen, and S. Novikov
Optical properties of silicon nanocrystals in silica: Results from spectral filtering effect, m-line technique, and x-ray photoelectron spectroscopy
J. Appl. Phys. 104, 104316 (2008)

II. L. Khriachtchev, **T. Nikitin**, R. Velagapudi, J. Lahtinen, and S. Novikov
Light-emission mechanism of thermally annealed silicon-rich silicon oxide revisited: What is the role of silicon nanocrystals?
Appl. Phys. Lett. 94, 043115 (2009)

III. **T. Nikitin**, L. Khriachtchev, M. Räsänen and S. Novikov
Optical memory of silicon nanocrystals with submicron spatial resolution and very high thermal stability
Appl. Phys. Lett. 94, 173116 (2009)

IV. L. Khriachtchev, **T. Nikitin**, M. Räsänen, A. Domanskaya, S. Boninelli, F. Iacona, A. Engdahl, J. Juhanoja, and S. Novikov
Continuous-wave laser annealing of Si-rich oxide: A microscopic picture of macroscopic Si-SiO_2 phase separation
J. Appl. Phys. 108, 124301 (2010)

V. **T. Nikitin**, K. Aitola, S. Novikov, M. Räsänen, R. Velagapudi, J. Sainio, J. Lahtinen,
K. Mizohata, T. Ahlgren, and L. Khriachtchev
Optical and structural properties of silicon-rich silicon oxide films: Comparison of ion implantation and molecular beam deposition method
Phys. Status Solidi (a) 208, 2176 (2011)

VI. **T. Nikitin**, M. Kemell, E. Puukilainen, S. Boninelli, F. Iacona, M. Räsänen, M. Ritala, S. Novikov, and L. Khriachtchev
Surface fingerprints of individual silicon nanocrystals in laser-annealed Si/SiO_2 superlattice: Evidence of nanoeruptions of laser-pressurized silicon
J. Appl. Phys. 111, 124302 (2012)

VII. **T. Nikitin**, R. Velagapudi, J. Sainio, J. Lahtinen, M. Räsänen, S. Novikov, and L. Khriachtchev
Optical and structural properties of SiO_x films grown by molecular beam deposition: Effect of the Si concentration and annealing temperature
J. Appl. Phys. 112, 094316 (2012)

VIII. **T. Nikitin**, M. Kemell, E. Puukilainen, M. Räsänen, M. Ritala, S. Novikov, and L. Khriachtchev
Continuous-wave laser annealing of a Si/SiO_2 superlattice: Effect of the ambient atmosphere and exposure period
Submitted to Science of Advanced Materials

The candidate, Timur Nikitin, has done all photoluminescence, Raman, and transmission/reflection measurements in publications III-VIII and a part of experimental work in publications I and II. He extracted optical parameters and performed the analysis based on the effective medium approximation in publication VII. He comparatively analyzed the XPS, SEM, AFM, and TEM results obtained by the partners in publications III–VIII. The candidate participated in preparation of the publications (especially V,VII, and VIII).

Other publications:

1) S. Novikov, J. Sinkkonen, T. Nikitin, L. Khriachtchev, M. Räsänen, and E. Haimi, *Free-standing SiO_2 films containing Si nanocrystals directly suitable for transmission electron microscopy,* Microelectron. J. 39, 518 (2008)
2) O. Lehtinen, L. Sun, T. Nikitin, A. V. Krasheninnikov, L. Khriachtchev, J. A. Rodríguez-Manzo, M. Terrones, F. Banhart, and J. Keinonen, *Ion irradiation of carbon nanotubes encapsulating cobalt crystals,* Physica. E, 40, 2618 (2008)
3) Y. Tian, H. Jiang, J. v. Pfaler, Z. Zhu, A. G. Nasibulin, T. Nikitin, B. Aitchison, L. Khriachtchev, D. P. Brown, E. I. Kauppinen, *Analysis of the size distribution of single-walled carbon nanotubes using optical absorption spectroscopy,* J. Phys. Chem. Lett. 1, 1143 (2010)
4) O. Lehtinen, T. Nikitin, A. V. Krasheninnikov, L. Sun, L. Khriachtchev, F. Banhart, T. Terao, D. Golberg, J. Keinonen, *Ion irradiation of multi-walled boron nitride nanotubes,* Phys. Status Solidi C 7, 1256 (2010)
5) Y. Tian, A. G. Nasibulin, B. Aitchison, T. Nikitin, J. v. Pfaler, H. Jiang, Z. Zhu, L. Khriachtchev, D. P. Brown, and E. I. Kauppinen, *Controlled Synthesis of Single-Walled Carbon Nanotubes in an Aerosol Reactor,* J. Phys. Chem. C 115, 7309 (2011)
6) O. Lehtinen, T. Nikitin, A V Krasheninnikov, L. Sun, F. Banhart, L. Khriachtchev, and J. Keinonen, *Characterization of ion-irradiation-induced defects in multi-walled carbon nanotubes,* New J. Phys. 13, 073004 (2011)
7) I. Miklós Szilágyi, E. Santala, M. Heikkilä, M. Kemell, T. Nikitin, L. Khriachtchev, M. Räsänen, M. Ritala, and M. Leskelä, *Thermal study on electrospun polyvinylpyrrolidone/ammonium metatungstate nanofibers: optimising the annealing conditions for obtaining WO_3 nanofibers,* J. Therm. Anal. Calorim. 105, 73 (2011)
8) L. Sirleto, M. A. Ferrara, T. Nikitin, S. Novikov, and L. Khriachtchev, *Giant Raman gain in silicon nanocrystals,* Nat. Commun. 3, 1220 (2012)
9) I. M. Szilagyi, E. Santala, M. Heikkila, V. Pore, M. Kemell, T. Nikitin, G. Teucher, T. Firkala, L. Khriachtchev, M. Räsänen, M. Ritala, and M. Leskela, *Photocatalytic Properties of WO_3/TiO_2 Core/Shell Nanofibers prepared by Electrospinning and Atomic Layer Deposition,* Chem. Vap. Deposition 19, 149 (2013)
10) I. M. Szilagyi, G. Teucher, E. Harkonen, E. Farm, T. Hatanpaa, T. Nikitin, L. Khriachtchev, M. Räsänen, M. Ritala, and M. Leskela, *Programming nanostructured soft biological surfaces by atomic layer deposition,* Nanotechnology 24, 245701 (2013)
11) T. Nikitin, S. Novikov, and L. Khriachtchev, *Giant Raman gain in annealed silicon-rich silicon oxide films: Measurements at 785 nm,* Appl. Phys. Lett. 103, 151110 (2013)

1 Introduction

Many limitations of modern electronic devices may be overcome by implementing photonics into electronics.[1-4] Integration of silicon-based photonics with CMOS technology is a promising approach since it gives the possibility to merge electronics and photonics efficiently in the same chip.[5-9] Many optical functions such as, for example, light sources, amplifiers, waveguides, modulators, memory, and detectors should be achieved in order to fulfil this integration.[1,7] Realization of a true monolithically fabricated injection Si laser with a small size is a particularly challenging task.[7] The reason lies in the low light-emitting efficiency of bulk silicon due to its indirect band gap (~1.1 eV), which implies long radiative times (~ms) and therefore, mostly non-radiative recombination of the excited carriers. The efficiency of the light emission can be enhanced by increasing the overlap of the electron and hole wavefunctions via, for example, spatial confinement.[10-13] The unusual properties of Si structures are observed when the size is less than the free exciton Bohr radius of 4.3 nm in bulk Si.[14] This quantum confinement (QC) effect leads to the following main changes in the material properties: i) a decrease of the non-radiative recombination rates due to spatial confinement of the carriers; ii) an increase of the radiative probability due to delocalization of the wavefunctions in the momentum space, which increases the electron-hole wavefunction overlap; iii) a shift in the emission wavelength to the visible region due to an increase of the band gap, which is controlled by the Si nanostructure size.[1]

1.1 Light emission from Si nanocrystals

Porous Si (p-Si) is the first example of Si-based material with an increased luminescence efficiency. Strong room-temperature photoluminescence (PL) in visible region (~1.5 eV) was discovered from this material by Leigh Canham in 1990.[15] Visible luminescence ranging from green to red in color was soon reported by Canham et al. for other p-Si samples and ascribed to the quantum size effects in Si wires of width ~3 nm,[16] and by other researchers.[17,18] The blue shift of the PL and of optical absorption with increasing porosity (decreasing Si nanocluster sizes) provided the first important evidence that the QC plays an important role in light emission from p-Si. This blue shift is a result of the band gap expansion controlled by the Si nanostructures sizes.[13,19]

It was soon understood that the nature of the surface localized states of small Si crystallites has a great influence on the light emission.[20,21] Wolkin et al. showed that for hydrogen-passivated p-Si, recombination occurs via free exciton states for all crystallite sizes and follows the expected QC behavior.[22] Ledoux et al. studied Si nanocrystals (Si-nc) prepared by pulsed CO_2 laser pyrolysis of silane in a gas flow reactor and deposited on a substrate.[23] It was observed that the PL band blue-shifted as the size of the particles decreased from 8 to 2.5 nm. This dependence clearly follows the QC model. The QC mechanism operates also for alkane-terminated Si-nc. Hannah et al. convincingly demonstrated using pressure-dependent PL studies that the PL emission arises from core-

states of Si-nc with indirect-gap transition.[24] The same PL mechanism was also reported to operate for Si-nc in silicon-nitride films.[25,26]

Another attractive Si-based material, which is the focus of the present thesis, is composed of Si-nc embedded in a SiO_2 matrix. This material is chemically and mechanically more stable compared to p-Si and also emits light in the visible region. Studies of Si-nc in SiO_2 have been stimulated by the observation of optical gain in this material.[27,28] In addition to PL, electroluminescence in visible region from p-Si and from Si-nc in SiO_2 has also been reported.[29,30] The origin of the PL from Si-nc in a SiO_2 matrix is quite controversial. The conclusions on the mechanism of the light emission from oxidized p-Si seem to be relevant to Si-nc in SiO_2. Studies by Wolkin and coworkers of oxidized p-Si showed that the light-emitting centers can involve Si=O covalent bonds located on the surface of p-Si.[22] For oxygen-passivated Si clusters, a stabilized electronic surface state is formed on a Si=O covalent bond and different recombination mechanisms can operate depending on the crystallite size. For larger sizes (>3 nm), recombination occurs via free excitons since the band gap is not wide enough to stabilize the Si=O surface state; for intermediate sizes (~2.5 nm), recombination involves a trapped electron localized on the Si atom of the Si=O bond and a free hole; and for smaller sizes (<2 nm), recombination is via trapped excitons. This model was soon supported by theoretical calculations.[31] Similarly, the PL of Si-nc (sizes >3 nm) in SiO_2 was also ascribed to the QC effect.[32-35] On the other hand, the importance of the Si-nc/SiO_2 interface in the light-emitting properties has been stressed[36-39] and, in particular, the defect origin of the PL has been discussed.[38,40-44] Godefroo et al. have convincingly demonstrated that defects are the dominant source of the 1.5-eV PL.[45] The authors could switch the PL mechanism between the QC and defect mechanisms by passivation with hydrogen and ultraviolet illumination, respectively. Further discussion of the PL mechanism based on our results for SiO_x ($x < 2$) films can be found in section 3.1.2.

1.2 Optical and structural properties of Si-nc in silica

Optoelectronic applications of Si-based materials require knowledge of their optical and structural properties. For Si-rich silicon oxide SiO_x ($x < 2$) films prepared by plasma enhanced chemical vapor deposition (PECVD), the energy-filtered transmission electron microscopy (EFTEM) studies have demonstrated that the Si–SiO_2 phase separation starts after annealing at 900 °C for 1 hour in N_2 atmosphere when Si clusters become visible in an oxide matrix.[46] The dark-field (DF) TEM technique reliably shows that the Si clusters are amorphous for annealing temperatures 900–1000 °C, and their crystallization begins at 1100 °C. Higher annealing temperatures promote further crystallization of the Si clusters. The Si-nc sizes as a function of the annealing temperature and Si content have been studied for samples prepared by different deposition methods. For samples prepared by PECVD, the TEM results indicate that the Si-nc sizes increase with the increasing annealing temperature for a given Si content and with the Si content for a given annealing temperature.[47] The increase of the Si-nc sizes with the annealing temperature is also observed for SiO_x films prepared by magnetron sputtering (MS).[48] For implanted SiO_x films, it is shown that the

nucleation and pure growth stages of the nanocrystal population are almost over after 1 min of annealing at 1100 °C in N_2.[49] For longer annealing periods, the Si-nc grow due to coalescence or Ostwald ripening process.[49,50]

The control of optical constants (refractive index and absorption coefficient) of SiO_x films by varying the Si content and annealing temperature is important for optoelectronic applications. Several methods have been employed to study the optical constants of different materials containing Si-nc. These methods include, for example, optical ellipsometry[51-53] and m-line measurements.[54-56] The analysis of the optical properties often uses the Bruggeman effective-medium approximation.[57-59] The Tauc-Lorentz model provides optical constants of Si-nc deposited on a substrate.[59] The results show that the optical properties of Si-nc are quite different from those of amorphous and crystalline Si. It has been found that at a given wavelength, the refractive index increases for larger Si-nc[51] and the Si content.[52] Chen et al. have developed a quantitative approach of obtaining depth profiles of the optical constants.[58] Moreno et al. report that the refractive index of Si-nc is lower than that of amorphous and crystalline bulk Si.[57] They also conclude that the refractive index is rather independent on the Si clusters sizes (3.6–4.6 nm) and depends mostly on the crystalline or amorphous structure of the Si clusters. At a given wavelength, the absorption coefficient of annealed SiO_x films prepared by MS and PECVD increases with the Si content.[53,60,61] This can be explained by the growth of Si-nc i.e. increasing density of Si–Si bonds.[60] The growth of Si-nc also leads to an increase of absorption in p-Si[62] and in SiO_x films prepared by Si ion implantation.[57] For a fixed Si content, the absorption coefficient of films prepared by MS and PECVD decreases with the increasing annealing temperature, which is due the amorphous-to-crystalline transition of Si in the samples.[60]

Another method of measuring the refractive index and thickness of a SiO_x film is the PL-filtering effect. A silicon oxide layer containing Si-nc on a silica substrate forms a planar waveguide. Spectral filtering of the PL occurs when the PL spectrum is measured from the waveguide edge along the film surface. This effect was first found in a Si/SiO_2 multilayer (superlattice, SL) film on silica substrate[28] and then also in SiO_x films ($x < 2$).[56,63-65] The detailed description of this effect is presented in section 2.3.1.

For SiO_x/SiO_2 SLs prepared by MS, negative optical birefringence (~1 %) was observed, which has been explained by the presence of SL structure.[54,55] In contrast, SiO_x prepared by molecular beam deposition method (MBD) show a positive birefringence up to 8 % explained by non-spherical shape of the Si-nc.[56]

The band gap of SiO_x films containing Si-nc is usually estimated from the absorption spectra using the Tauc relation.[49,51,60,66-68] A study of Si-nc deposited on a silica substrate shows that the electronic band structure of Si-nc is quite different from that of bulk silicon and that the band gap energy increases as the Si-nc size decreases.[59] The latter observation was explained by the QC effect. The increase of the band gap for smaller Si-nc sizes was also observed for implanted SiO_x samples.[49,51] The absorption threshold is blue-shifted for smaller Si-nc, which also indicates the influence of the QC effect on the Si-nc band gap.[60,62,68,69]

1.3 Theoretical studies of optical properties of Si-nc

In agreement with experimental observations, theoretical simulations of isolated hydrogen-passivated Si nanostructures show that the band gap and the PL peak position change according to the QC theory.[13,19] The situation changes for oxidized Si-nc.[70] Theoretical studies highlight the importance of the interface region between the Si-nc and the silica matrix for the light-emitting properties.[71,72] The absorption edge tends to red-shift due to formation of Si=O or Si–O–Si bonds at the Si/SiO_2 interface.[73-75] Luppi et al. considered small Si-nc (up to 1 nm in diameter) by applying *ab initio* calculations.[76] In the case of the Si–O–Si bridge bond at the cluster surface, an emission peak at energy of about 1.5 eV was found. Importantly, PL in this region is often observed experimentally from silica films containing Si-nc. The calculated emission peak is red-shifted with respect to the absorptions peaks, which is also in agreement with the experimentally observed Stokes shifts between the absorption and PL spectra.

The surrounding matrix always produces some strain on the nanocrystal, especially at the Si/SiO_2 interface, and that this strain depends on the oxidation degree.[77,78] The amount of strain affects the bad gap, which also shows an oscillating behavior with the Si-nc size, not strictly following the QC rule.[77] Moreover, the disorder of nanoclusters has a large effect on their optoelectronic properties. In particular, the amorphization reduces the fundamental gap while increasing the absorption strength in the visible range.[79]

In a recent work, Guerra and Ossicini have calculated the recombination rates for different classes of Si-nc in the diameter range of 0.2–1.5 nm.[80] The authors also considered different conditions of passivation, strain, and symmetry in order to find the best conditions of radiative emission. As a result, they found that the smallest, highly oxidized, crystalline clusters are the most optically active Si/SiO_2 structures.

1.4 Fabrication of Si-nc

Si-nc in silica films can be prepared by a number of deposition methods such as, for example, MBD,[44,81] Si-ion implantation,[38,40,82,83] MS,[37,60,84,85] and PECVD.[47,60,84,86,87] Two types of architectures are most commonly prepared: a) SiO_x ($x < 2$) films[38,47,60,88,89] and b) SLs with SiO_x ($x < 2$) and SiO_2 layers (SiO_x/SiO_2,[45,85,90-92] Si/SiO_2[37,44,81,93-96] for $x = 0$). Si-nc are formed in these materials after furnace annealing above 1000 °C. Si and SiO_2 wafers are typically used as the substrates.

1.5 Laser annealing

Laser annealing is an interesting approach to change the structural and optical properties of Si-based materials. The heating effect of pulsed radiation is especially strong.[97] However, it can also be substantial for cw irradiation of free-standing porous films.[98] The same temperature effect of cw laser radiation was later observed in free-standing SiO_x films

containing Si-nc leading to a strong increase of the Raman signal of Si-nc.[95,99-101] Si-nc prepared by laser annealing show high compressive stress (~3 GPa), which is evidenced by an up-shift of the Raman band.[95] The compressive stress is formed in a solid silica matrix when the volume of Si-nc suddenly increases after its crystallization from the liquid phase. The high stress can be relaxed by irradiating the stressed Si-nc with lower laser power.[95] Free-standing films were used to obtain the above described laser-induced effects because for films on substrates the laser-induced heat is reduced due to thermal flux to substrate,[102] but still observable (section 3.1.4).[103]

1.6 Characterization techniques used in this study

The following techniques are the most commonly employed to characterize thin films containing Si nanostructures:

Photoluminescence (PL) spectroscopy is widely used to obtain information about electronic band structure and nature of defects and impurity centers in Si nanostructures. PL studies can be done with continuous-wave (cw) and pulsed lasers. In the latter case, the PL lifetimes can be measured, which provides information on carrier recombination processes.

Optical absorption. The absorption of films containing Si nanostructures is obtained by measuring transmission and reflection in ultraviolet (UV) and visible (VIS) regions using a broadband light source. The band gap of semiconductors can be obtained from the absorption spectra using the Tauc relation.[66] (section 2.3.5)

Raman spectroscopy is based on inelastic light scattering. It is fast and non-destructive method widely used to study nanostructured material. The shape of the Raman band of Si nanostructures depends on many parameters such as disorder, Si-nc shape and size distribution, strain, temperature, etc. In principle, by analyzing the Raman peak shape, these parameters can be estimated, provided some of them are known.

Transmission electron microscopy (TEM) is widely applied because of a reliable estimation of the Si-nc sizes. Two modes of TEM are also used: dark field TEM (DFTEM) and energy filtered TEM (EFTEM). DFTEM is sensitive to the presence of crystalline planes in the sample and it is therefore used to detect crystalline Si clusters. The estimation of the Si-nc mean sizes with this mode is approximate (especially for very small sizes) and the Si-nc volume density cannot be calculated precisely. EFTEM mode provides a chemical mapping with a very high spatial resolution. This technique can reliably detect both amorphous and crystalline phases of Si.

In s*elected area diffraction* (SAD), a diffraction pattern is made under parallel beam of high-energy electrons illuminating a thin specimen inside transmission electron microscope. In this case, atoms of the specimen act as a diffraction grating to a wave of electrons. SAD of nanostructures is used to identify their amorphous or crystalline state.

Infrared spectroscopy (IR) spectroscopy provides information about chemical bonding in the material.

X-ray photoelectron spectroscopy (XPS) measurements provide detailed information about the elemental composition, chemical and electronic states of the elements of the material. Since only a thin layer of the sample (usually 1–10 nm) can be investigated with

this method, the sample is sputtered with Ar^+ ions to gain information about the bulk material.

M-line technique is based on the optical coupling between a high refractive index prism and the film to be characterized. The prism-film coupler is a device allowing an accurate measurement of the spectrum of the film propagating modes from which the refractive index and the thickness of the film can be determined. The method is based on the principle of distributed coupling through evanescent fields to the modes of thin-film waveguide.

Atomic force microscopy (AFM) is used to characterize surfaces at extremely high resolution. A sharp tip is brought into close proximity with the sample to be analyzed. The interactions between the tip and sample surface are measured by monitoring the displacement of the free end of the attached cantilever. The resulting signal is transformed into a surface topography map.

In *scanning electron microscopy* (SEM), the sample is scanned with a focused beam of electrons. Different signals can be detected: electrons from the sample (secondary electrons), transmitted electrons, and X-rays, which provide information about the sample surface topography, composition, and the elemental composition of the material, respectively.

2 Experimental details and methods

2.1 Samples

2.1.1 Molecular beam deposition

Most of the samples for this study were prepared by MBD in the Aalto University (Finland) by Dr. S. Novikov. Samples containing areas with different Si contents as well as samples with constant Si content were prepared. The SiO_x films were deposited on round silica wafers (diameter ~7.5 cm) and had a Si content in the lateral direction.[I,VII] Therefore, such samples are called "optical wedges".[56,63,88,89] The advantage of optical wedges is that the areas with different Si contents are annealed under the same conditions and O/Si concentration ratio x can be continuously changed by selecting a proper film area. The samples were cut in slices (5–7 cm long and ~1 cm wide) along the Si content gradient and annealed at temperatures up to 1200 °C for 1 hour in nitrogen atmosphere in a furnace. For the study described in Ref. VII, x achieved in three samples varied from ~1.3 to ~1.98. Due to the deposition conditions, these films also have a thickness gradient (1.5–2.5 μm). Two optical wedges had a variation of parameter x with respect to two central values (~1.65 and 1.7) and one SiO_x sample had a constant composition (x ~1.55).[I] The Si/SiO_2 SL films were made of 125 or 500 pairs of 2-nm-thick Si and SiO_2 layers, yielding the total film thicknesses 0.5 or 2 μm, respectively. The free-standing films were prepared from the samples without Si gradient annealed at 1100 °C in nitrogen atmosphere in a furnace by chemical etching of the Si substrate.[104,IV,VI,VIII]

2.1.2 Si-ion implantation

One sample was made by Si-ion implantation into a silica substrate in the Accelerator Laboratory (University of Helsinki).[V] The implantation of Si ions into a silica plate was done with different energies (30, 56, 98, 160, 250, and 400 keV) and doses to achieve a nearly constant Si excess in the SiO_x layer with a thickness of ~750 nm. The O/Si concentration ratio x was estimated by XPS to be ~ 1.8. The implanted sample was annealed at various temperatures up to 1200 °C for 1 hour in N_2 atmosphere.

2.2 Equipment

The main analytical techniques used in the Laboratory of Physical Chemistry are Raman, PL, and IR-visible-UV absorption methods. Two setups were used to acquire the Raman and PL spectra. The first setup consists of an argon-ion laser (488 nm, Melles Griot 543-AP-A01), a spectrometer (Acton SpectraPro 500I), and a charge-coupled device camera

(Andor InstaSpec IV). The laser beam for this setup was focused with a lens to a spot with a diameter of ~40 μm. The second setup allowed us to carry out micro-Raman and micro-PL measurements. It consists of a confocal microscope (LabRAM HR800, Horiba Jobin Yvon) equipped with an Ar-ion laser (488 nm). The size of the laser spot in these measurements was down to ~1 μm. For both setups, the spectral resolution of the Raman and PL measurements was ~2 cm^{-1} and 10 cm^{-1}, respectively. The Raman bands of the films annealed at temperatures ≥1000 °C were fitted with two or three Gaussians. The position of the Raman band of Si-nc was obtained from the position of the higher-frequency Gaussian (~518–530 cm^{-1}). The PL spectra were corrected for the spectral sensitivity of the apparatus. The Raman and PL intensities were normalized by the effective thickness $\int e^{(-2\alpha x)}dx$ and $\int e^{(-\alpha x)}dx$, respectively, assuming the same absorption coefficients for the laser and Raman light and neglecting the absorption for the PL at ~800 nm.[94]

Laser annealing of free-standing films was performed using a TEM_{00} beam of an Ar-ion laser (488 nm, power up to 110 mW at the sample) focused to spots with diameters ranging from ~1 to ~40 μm. The exposure time was mainly ~1 s, but 10-ms and 100-s exposures were also used.

The absorption coefficients, α, were obtained from the transmission and reflection spectra,[105] recorded with a fiber-optics spectrometer (SD2000, Ocean Optics) and a broadband light source (DH-2000, Top Sensor Systems) or by directly measuring transmitted and reflected laser light using a power meter (NOVA II, OPHIR). Micro-transmission measurements of the 488-nm light in the LabRAM microscope were done with a large-area photodiode placed behind the sample. M-line measurements were carried out with a 633-nm He-Ne laser.

Additional analytical methods were available from cooperation: XPS[I,II,V,VII] including that with high spatial resolution,[IV] Fourier-transform infrared spectroscopy (FTIR) with high spatial resolution,[IV] TEM including bright-field scanning (BF-S) TEM and EFTEM,[IV,VI] electron energy loss spectroscopy (EELS),[IV] SEM and energy-dispersive X-ray spectroscopy (EDS),[VI,VIII] AFM,[VI,VIII] and m-line measurements.[I]

2.3 Methods

2.3.1 PL-filtering effect

The method to measure optical properties of the SiO_x films utilizes the PL-filtering effect.[I] The PL-filtering is observed when measuring the PL spectra in a direction along the film surface. In this case, narrow and polarized spectral peaks are detected (Figure 1a). The PL-filtering was observed in silica layers containing Si-nc, prepared with various methods (Si-rich silica, Si implantation, and Si/SiO_2 superlattices).[28,56,63-65,89,96,99] The PL-filtering effect was interpreted in terms of delocalization of guided modes near the cut-off frequency.[56,63,89,96] The minimal losses occur near the cut-off frequencies, when the delocalized light travels mostly in the transparent substrate rather than in the film, where

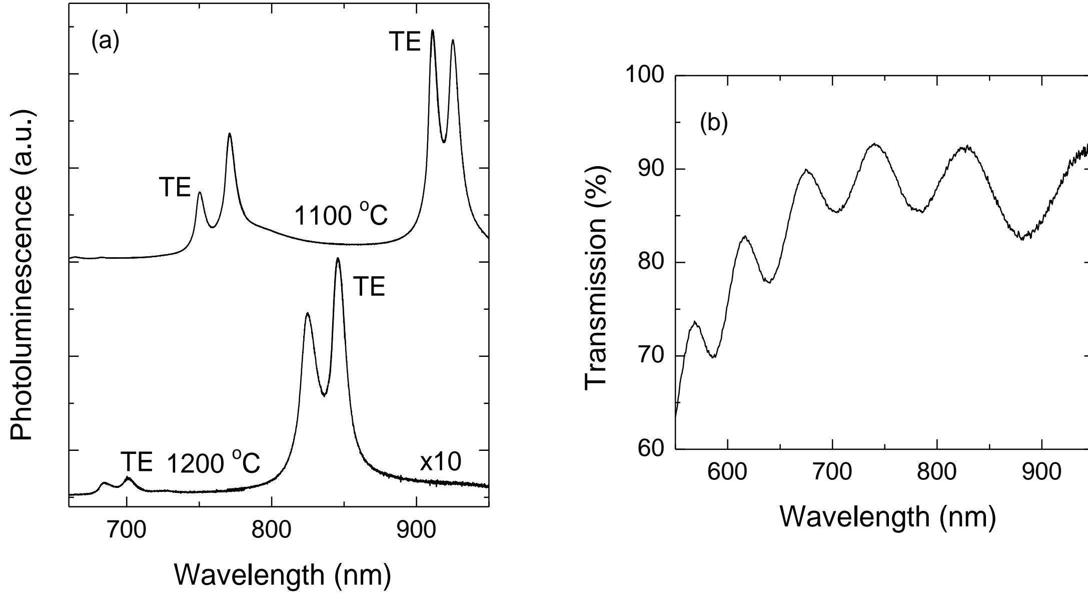

Figure 1 *(a) Cut-off spectra of $SiO_{1.5}$ film annealed at 1100 and 1200 °C, measured from the sample edge along the waveguide surface. The excitation spot was at a distance of several millimeters from the sample edge. The positions of the TE peaks are marked and the other bands have the TM polarization. TE and TM peaks have polarization parallel and perpendicular to the film surface, respectively. (b) Transmission spectrum of the $SiO_{1.5}$ film annealed at 1100 °C.*

the absorption is much stronger. Thus, the narrow peaks seen in the PL spectra obtained in the waveguiding direction correspond to the cut-off wavelength. The mode localization is a function of the generalized frequency parameter written for an asymmetrical waveguide in the form:

(1) $$V = 2\pi\sqrt{(n_1^2 - n_2^2)}\, d/\lambda\,,$$

where n_1 and n_2 are the refractive indexes of the film and the substrate, respectively, d is the film thickness, and λ is the wavelength. This equation was obtained assuming weak-guiding approximation $(n_1\text{-}n_2) \ll 1$.[106] For the cut-off condition $V = (2m + 1)\pi/2$, equation (1) yields the cut-off wavelengths.

Figure 1(b) shows a typical transmission spectrum of an annealed SiO_x film (x ~ 1.55) on a silica substrate. The spacing of the interference patterns (in cm^{-1}) can be written as

(2) $$\delta v = \frac{1}{2n_1 d},$$

which provides the optical thickness (*nd*). The numerical information can be extracted from the transmission spectrum by fitting it, for example, with the following empirical function:

(3) $$T(\lambda) = P_7 + P_1\left(1 - \frac{P_3}{\lambda - P_2}\right)\left[1 - P_4 \sin\left(\frac{P_5}{\lambda} + P_6\right)\right],$$

where T is transmittance, λ is the wavelength, and P_i are the fitting parameters.[89] In particular, the P_5 parameter is connected with the period of the oscillations, i.e. with the optical thickness. The refractive index relevant to the transmission is the TE refractive index. By using the equation (1) for the TE peaks and equation (2), the TE refractive index and layer thickness can be extracted.[63] Next, the obtained layer thickness together with the TM peak positions are used to calculate the TM refractive index. The obtained thickness is also used to calculate the absorption (extinction) coefficient from the transmission and reflection measurements.

The model described above is called a *simple model* as it uses a few simplifications: (i) equation (1) was derived using the weak-guiding approximation $(n_1 - n_2) \ll 1$ (this difference mainly affects the cut-off positions but not the interval between these positions),[106] (ii) the procedure uses only the spacing between the cut-off peaks disregarding their actual positions, (iii) the material dispersion was neglected, and (iv) a step-index profile was assumed for the refractive index.[I] To take the dispersion of the material into account, the transmission spectra were fitted with a function similar to equation (3) but containing an additional term describing the wavelength dependence of the spacing $\delta\nu$.[I] The corrected optical thickness was found. Equations (1) and (2) were then solved taking the dispersion correction into account. The results show that the dispersion corrections for refractive index and film thickness are within the experimental errors (Figure 2). The refractive index and thickness were also calculated using a model of reflection from a multilayer system,[107] which did not limit the refractive indexes (the exact equations).

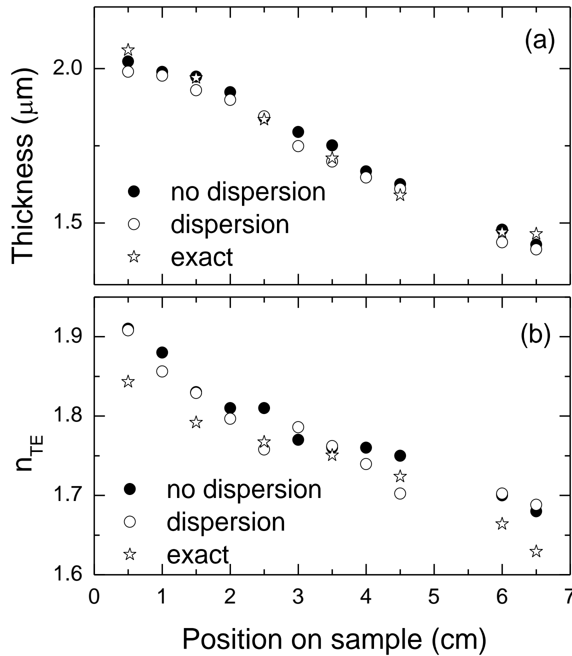

Figure 2 *Optical parameters of a SiO_x ($1.5 < x < 1.8$) film obtained with different models: neglecting dispersion (solid circles), taking dispersion into account (open circles), and using the exact equations[107] (stars).*

The analysis included both spacing and positions of the cut-off peaks. Equation (3) with the additional term describing the material dispersion was also used in this case.[I] Again, the differences from the simple model were within the experimental errors (Figure 2). Based on the XPS data for a $SiO_{1.55}$ film annealed at 1100 °C, it was concluded that the use of smooth index profile of the refractive index is not crucial to obtain good description of the delocalized cut-off modes. These results suggest that the simple model is sufficient to obtain adequate estimates of the refractive index and film thickness. The m-line measurements performed for SiO_x ($1.5 < x < 1.8$) film confirmed the values for the Si concentration and thickness gradient along the optical wedge obtained using the PL-filtering effect.

The PL-filtering effect was also interpreted in terms of substrate leaky or radiation modes of a planar waveguide.[64,65] In this model, the regular guided modes experience greater loss propagating over a macroscopic distance from the place of creation towards the sample edge. The most likely source of the loss is absorption and scattering from nanocrystals, as well as scattering from the "interface" between the core and cladding layers. In contrast, the beams responsible for generating the substrate modes travel shorter distances through the core region, and the substrate mode undergoes virtually no loss in traveling to the substrate facet. There seem to be no contradiction between descriptions based on mode delocalization and substrate leaky modes. In particular, both of these models explain the PL-filtering effect based on a smaller absorption in the substrate compared to the layer with Si-nc.

2.3.2 XPS spectra

In the case of SiO_x films, the Si 2*p* spectrum is fitted by several peaks to obtain the amounts of Si in different oxidation states. Three peaks were used to describe Si atoms bonded as in crystalline Si (elemental Si), "SiO" (mixture of various suboxides), and SiO_2 materials (Figure 3).[I,VII] More complicated fitting with five peaks can be used to obtain five oxidation states (elemental Si, Si_2O, SiO, Si_2O_3, and SiO_2) of Si in different materials.[108-110] For our samples, the fittings with three and five peaks give similar amounts of elemental Si and SiO_2.[VII] Moreover, the use of five fitting curves is problematic in the case of low Si content.

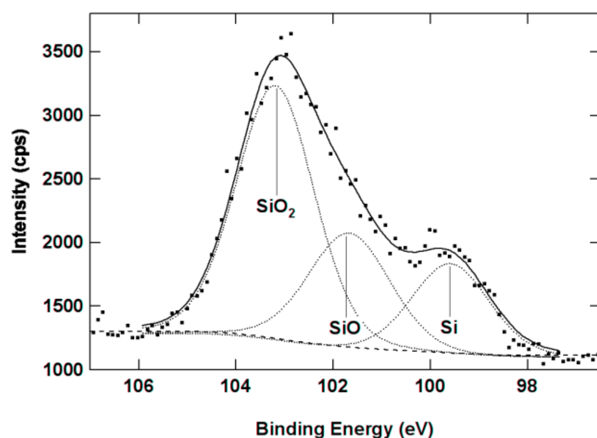

Figure 3 *Typical XPS spectrum of a SiO_x film fitted with three Gaussians corresponding to Si bonded as in elemental Si, SiO (mixture of suboxides), and SiO_2.*

2.3.3 Effective medium approximation

The effective medium approximation (Bruggeman theory) connects the effective dielectric constant with the dielectric constants of the three structural components and their volumetric fractions:[111]

$$a\left(\frac{\varepsilon_a-\varepsilon_m}{\varepsilon_a+2\varepsilon_m}\right)+b\left(\frac{\varepsilon_b-\varepsilon_m}{\varepsilon_b+2\varepsilon_m}\right)+c\left(\frac{\varepsilon_c-\varepsilon_m}{\varepsilon_c+2\varepsilon_m}\right)=0\ , \quad (4)$$

where *a*, *b*, and *c* are the volumetric fractions of each component, $\varepsilon_{a,b,c}$ are the corresponding dielectric constants, and ε_m is the effective dielectric constant. The effective medium approximation was employed to calculate the complex refractive index $n^* = n + ik$ (where *k* is the extinction coefficient) using the chemical compositions (Si, SiO, and SiO_2) obtained from the XPS measurements.[I,VII]

2.3.4. Temperature measurements

The laser-induced temperature can be measured *in-situ* using the intensities of the Stokes (I_S) and Anti-Stokes (I_{AS}) Raman bands (Figure 4) and the relation:

$$\frac{I_{AS}}{I_S}=Ae^{\left(-E_R/kT\right)}, \quad (5)$$

where E_R is the phonon energy and *A* is a correction coefficient.[100,112] The coefficient $A \sim 0.95$ was obtained by measuring the laser-induced temperature of a Si wafer as a function of the laser power and assuming room temperature in the irradiated volume at zero laser power. The measurements were done for the spectrometer Acton SpectraPro 500I and a charge-coupled device camera Andor InstaSpec IV.

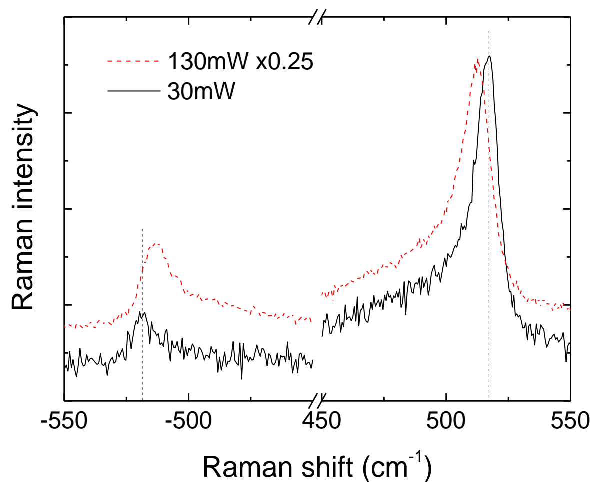

Figure 4 *Raman spectra of a $SiO_{1.3}$ film on silica substrate measured with two laser powers (30 and 130 mW through a ~40-µm laser spot). The spectra are vertically shifted for better presentation.*

2.3.5 Tauc law

According to the Tauc law, absorption spectrum (for $\alpha > 10^4$ cm^{-1}) obeys the following relation:[66,113]

(6) $$\sqrt{\alpha \cdot h\nu} = A(h\nu - E_{Tauc}).$$

A is a coefficient. Function $\sqrt{\alpha \cdot h\nu}$ was plotted versus $h\nu$ and fitted with a straight line. The value of the optical gap (E_{Tauc}) was obtained from the intercept of the linear fit with abscissa.

3 Results and discussions

3.1 Furnace-annealed SiO_x (x < 2) films on silica substrates

3.1.1 Correlation between optical and structural properties

In this section we describe the properties of SiO_x ($x < 2$) films for annealing temperatures (400–1200 °C) and Si contents (x from ~1.3 to ~1.96).[I,II,V,VII] The SiO_x films (thickness from ~1.5 to ~2.5 μm) were deposited on silica substrates by MBD.

The as-prepared films (annealed at 400 °C for better mechanical stability) with substantial Si content show a broad Raman band at ~470 cm^{-1}, which is characteristic for amorphous Si (Figure 5).[44,88,94,114,115] After annealing above 1000 °C, crystallization of the amorphous Si inclusions occurs as evidenced by the narrowing and upshift of the Raman band to ~518 cm^{-1} (Figure 5). For laser intensities below 10^3 W cm^{-2} at the sample, the Raman band position (518–519 cm^{-1}) is practically independent of the Si content and of the annealing temperature in the 1100–1200 °C range. According to the phonon confinement model,[116,117] this result suggests that the Si-nc sizes the most sensible to Raman spectroscopy do not change much. However, the Si-nc growth with increasing annealing temperature was observed for SiO_x films prepared by other deposition techniques.[47,48] For films with very small excess of Si ($x > 1.9$), the Raman bands of amorphous and crystalline Si are practically invisible, in qualitative agreement with the previous results.[44] The reason behind this is the low amount of properly coordinated Si atoms, i.e. Si atoms bonded with four "bulk" Si atoms for samples with low Si content. A similar explanation was applied in

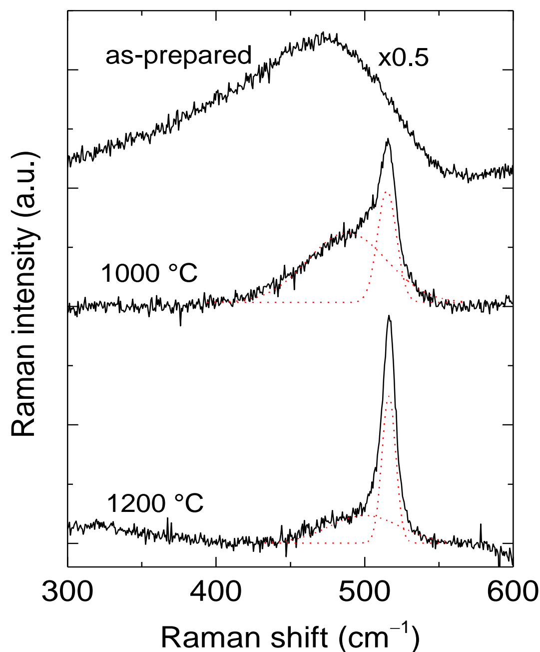

Figure 5 *Raman spectra of a $SiO_{1.75}$ film as-prepared and annealed at 1000 and 1200 °C (fitted by two Gaussians). The spectra are vertically shifted for better presentation. The Raman spectra were measured with laser intensity of ~10^3 W cm^{-2} at the sample.*

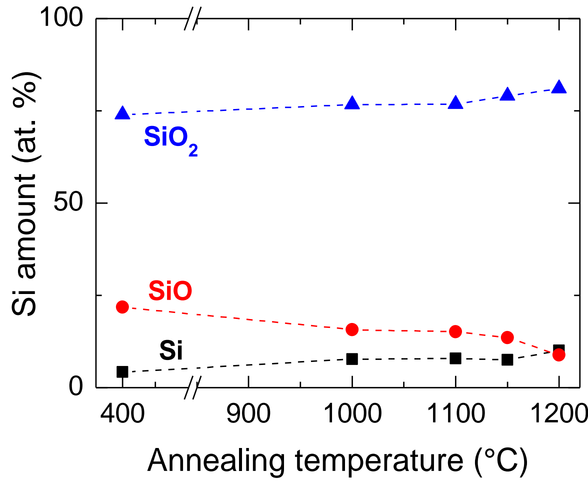

Figure 6 *Relative amounts of Si atoms bonded as in SiO_2 (triangles), SiO (circles), and elemental Si (squares) obtained from XPS as functions of the annealing temperature for x ~ 1.7.*

a study of amorphous Si/SiO_2 superlattices, where the Raman bands of amorphous Si were observed for thicker Si layers (≥2 nm) and the Raman-scattering cross section decreased for thinner Si layers.[94]

When the annealing temperature increases, the low-frequency shoulder in the Raman spectra responsible for disordered Si and/or small Si-clusters gradually decreases (Figure 5). However, even after annealing at 1200 °C the low-frequency Gaussian component of the Raman band for $SiO_{1.75}$ does not disappear completely and its area is comparable to that of the high-frequency component. As a possibility, small Si grains in silica matrix may be disordered even after annealing whereas larger Si grains are crystallized. It follows that the Si–SiO_2 phase separation is not complete at this temperature. The XPS results are in agreement with this conclusion (Figure 6). The Si–SiO_2 phase separation increases with the annealing temperature, which is evidenced by the increasing amount of elemental Si and SiO_2 and decreasing amount of SiO. However, a large proportion of suboxides (10–15 at.% for x = 1.7) is still detected after annealing at 1200 °C.[VII] This result indicates incomplete Si–SiO_2 phase separation in these materials.

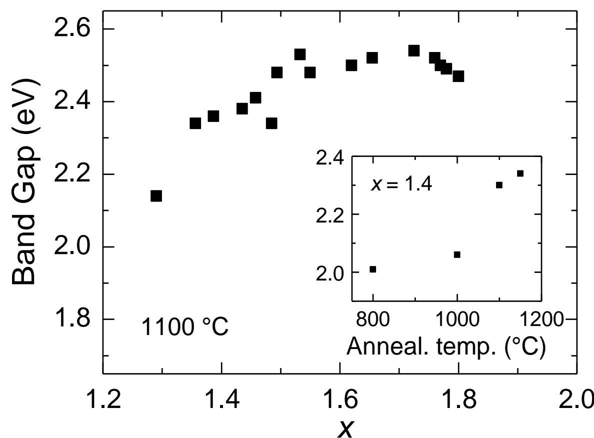

Figure 7 *Band gap of SiO_x films annealed at 1100 °C as a function of x. The insert shows the band gap of a $SiO_{1.4}$ film as a function of the annealing temperature.*

Additional information about the properties of SiO_x films can be obtained from the analysis of the band gap. For a given annealing temperature (from 900 to 1200 °C) the band gap of SiO_x films increases as the Si content decreases.[VII] In particular, for annealed at 1100 °C, when x increases from 1.3 to 1.8, the band gap increases from 2.2 to 2.6 eV (Figure 7), meaning that the Si-nc sizes somewhat decrease. According to the *ab initio* calculations for Si-nc with oxygen bonds at the Si/SiO_2 interface, the obtained band gap change (2.2–2.6 eV) corresponds only to a marginal change of Si-nc sizes, the average size being ~1 nm.[118] On the other hand, the position of the maximum of the Raman bands at 518–519 cm^{-1} corresponds to larger Si-nc sizes (3–4 nm),[116,117] and this value is supported by TEM measurements of similar materials.[104] These different estimates can be connected with low sensitivity of Raman and TEM methods to very small Si grains. The low-frequency Raman scattering at 490–500 cm^{-1} can be contributed by smaller Si-nc (1–2 nm) that may be partially disordered, which corresponds to the Si-nc sizes obtained from the band gaps. It should also be mentioned that the band gap of Si clusters is a complex function of a number of parameters in addition to the size, such as the crystallinity, strain due to the silica matrix, and degree of oxidation.[77,79] Moreover, the Tauc law is generally applicable for amorphous semiconductors with absorption coefficients $>10^4$ cm^{-1}.[66] Thus, the band gaps obtained by applying the Tauc law to crystalline Si grains with lower absorption may be somewhat inaccurate.

The band gap of SiO_x (x ~ 1.4[VII] and x ~ 1.8[V]) films was found to increase with the annealing temperature (see insert to Figure 7). This increase can be explained by amorphous-to-crystalline transitions of Si clusters rather than by a decrease of their sizes, following the discussions by Mirabella et al.[60] Indeed, the Si-nc sizes should rather increase with the annealing temperature[47,87] even though this increase for samples prepared by MBD seems to be minor as suggested by the independence of the Raman band positions on the annealing temperature.

By varying the Si content and annealing temperature, one can control optical properties

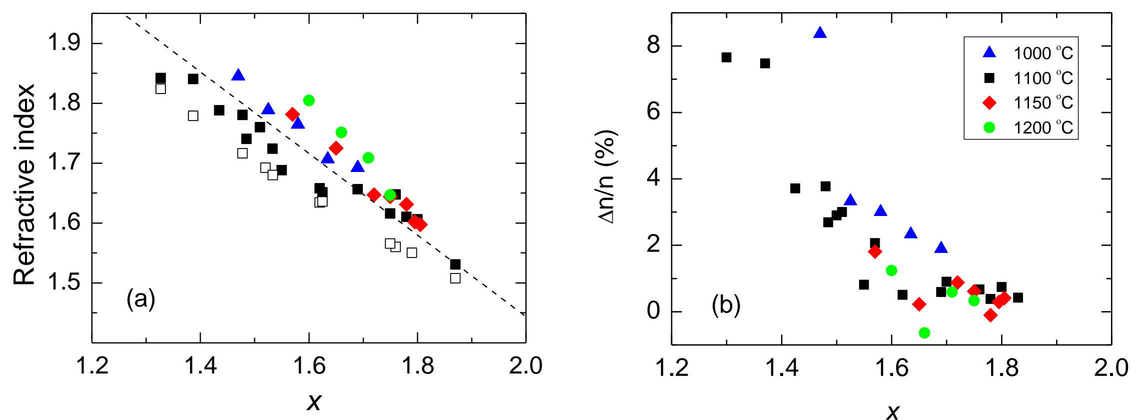

Figure 8 *(a) TE refractive index and (b) birefringence for annealing at 1000 °C (triangles), 1100 °C (squares), 1150 °C (diamonds), and 1200 °C (circles) as a function of x. The open squares are the values obtained using the effective medium approximation and the XPS results for annealing at 1100 °C. The dashed line is a guide for the eye.*

such as refractive index and absorption coefficient of SiO_x films, which is useful for optoelectronic applications. For a given annealing temperature, the refractive index of SiO_x films increases with the Si content (Figure 8a)[VII] as reported previously.[56,89] Extrapolation of the present data to $x = 2$ yields the refractive index that is close to that of silica (1.456), which is a good verification of our results. The obtained values are also in agreement with other experimental results for annealing at 1100 °C, $\lambda = 632$ nm, and $x \sim 1.38$–1.63.[57] For a given x, the refractive index typically decreases upon annealing at temperatures from 1000 to 1100 °C but increases in the 1100–1200 °C annealing temperature range.[VII]

The measured refractive index was compared with the values obtained using the effective medium approximation and the chemical compositions measured by XPS. The results are presented in Figure 8a for 1100 °C (open symbols) and in Table 1 for x~1.75,[I,VII] and the agreement is reasonably good. The small discrepancy can be due to the applied model and its limitations (the model taking dispersion into account, see section 2.3.1) as well as the possibility that the refractive indexes of nanostructures are different from those of the bulk materials (used in equation (4)). Moreover, the model used in the XPS analysis, in which the mixture of different suboxides constitutes the SiO component, can also contribute to the error.

The SiO_x films show optical birefringence.[56] The classical theory of an isotropic asymmetrical planar waveguide predicts that the cutoff positions for the TE modes (with polarization parallel to the film) are at longer wavelengths than the TM cutoff positions (with polarization perpendicular to the film).[106,119] However, the opposite spectral order between the TE and TM peaks was found for some samples as demonstrated by the upper spectrum in Figure 1a. The reversed order of the TE and TM peaks was explained assuming positive optical birefringence.[56] Our results confirm the conclusion of Ref. 56 that the optical birefringence is higher for SiO_x films with higher Si content and lower annealing temperature (Figure 8b).[VII] Similar values for birefringence were also obtained by m-line measurements for an optical wedge.[I] The birefringence was explained by non-spherical shape of Si-nc,[56] which were also observed by TEM in similar materials.[120]

Table 1 *Experimental refractive indexes n and absorption coefficients α of a $SiO_{1.75}$ film for different annealing temperatures T_{ann} and the estimates for the refractive indexes and extinction coefficients from the effective medium approximation.*

T_{ann} (°C)	n_{exp}	α_{exp} (10^4 cm^{-1})	n_{est}	k_{est}(SiO)	k_{est}(Si)
400	-	1.57	1.575	0.45	1.25
900	-	0.56	1.57	0.07	1.25
1000	1.64[a]	0.134[a]	1.56[a]	0	0.77
1100	1.61	0.126	1.56	0	0.53
1150	1.64	0.120	1.565	0	0.535
1200	1.67	0.128	1.57	0	0.48

[a]Obtained by extrapolation of the data to $x = 1.75$

The absorption coefficient of the SiO_x films was analyzed using the effective medium approximation and the XPS data, which provided further insight on the nanostructure of the thin films (Table 1).[I,VII] For as-prepared (annealed at 400 °C) $SiO_{1.75}$ film, if the extinction coefficient of amorphous Si ($k = 1.25$) is used for the elemental Si, the extracted extinction coefficient of the SiO phase (0.45) is much larger than the value for bulk SiO (0.055). This discrepancy would be smaller if the amount of elemental Si was underestimated by XPS and/or the extinction coefficient of nanoscale amorphous Si was larger than that of bulk amorphous Si. However, this discrepancy practically disappears for the sample annealed at 900 °C when our estimates agree with the extinction coefficients of bulk SiO and amorphous Si. High transparency of the nanoscale-suboxide component is found for films annealed above 1000 °C, in contrast to the corresponding SiO bulk material. The high transparency of suboxide is probably connected with its nanoscale structure.

As the annealing temperature increases, the calculated extinction coefficient of elemental Si decreases (Table 1), which is interpreted in terms of gradual crystallization of Si.[I,VII] However, this process in not complete even after annealing at 1200 °C, since the calculated extinction coefficient (0.48 for $x = 1.75$) is much larger than that of crystalline Si (0.079); thus, silicon is partially disordered.[87] This “disordered” Si should differ from ordinary amorphous Si because no Raman bands at 470 cm^{-1} are present for the films annealed above 1000 °C. Instead, the disordered Si grains may contribute to the Raman scattering at 490–500 cm^{-1}, which is present in Raman spectra of SiO_x films annealed up to 1200 °C (Figure 5).[VII] As a possibility, small Si grains in silica matrix may be disordered even after annealing whereas larger Si grains are crystallized. The presence of this disordered Si may explain the surprisingly large absorption of annealed SiO_x films.[I] Moreover, the optical properties of bulk and nanoscale silicon may differ, and the absorption by SiO inclusions cannot be completely excluded. This explanation of the relatively large absorption coefficient of annealed SiO_x films is quite speculative, and additional experimental data are required to draw more accurate conclusions.

The absorption coefficient and the integrated Raman intensity of Si-nc are nearly linear functions of the amount of elemental Si obtained by XPS (see Figure 9 for absorption),[I,VII]

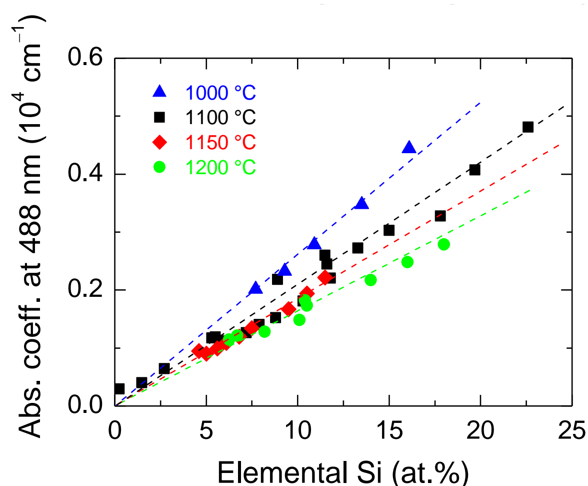

Figure 9 *Absorption coefficient at 488 nm for annealing at 1000 °C (triangles), 1100 °C (squares), 1150 °C (diamonds), and 1200 °C (circles) as a function of elemental Si.*

in agreement with the previous results.[88] It follows that elemental Si determines the absorption coefficient and the Si-nc Raman signal of SiO_x films. A similar conclusion was made for SiO_x films deposited by MS.[121] On the other hand, we have obtained that the Raman scattering cross-section of elemental Si in SiO_x films prepared by MBD is about three times smaller compared to that of crystalline Si. This can be explained by several factors.[VII] Ultra-small Si-nc (diameters <2 nm) may be invisible by Raman spectroscopy due to low amount of "properly" coordinated Si present in the annealed SiO_x films. The interaction with a SiO_2 matrix can change the coordination of Si-nc, and this effect is stronger for smaller Si particles. In principle, the broad band gap of Si-nc may affect the Raman cross-section due to the resonance effect. Finally, the complex character of interaction of light with Si-nc embedded in SiO_2 is not well understood. The present data is not enough to give a more reliable interpretation of these observations.

3.1.2 Photoluminescence of the MBD samples

For SiO_x films annealed up to 900 °C, weak PL is observed at 650–750 nm (Figure 10a), which is usually assigned to different thermodynamically unstable radiative defects, for instance, nonbridging oxygen-hole centers or E′-type defects.[49,83,122-124] After annealing above 900 °C, the maximum of the PL shifts towards longer wavelengths (~800 nm) and its intensity strongly increases (Figure 10),[V,VII] which agrees with numerous literature reports.[46,69,84,87,92] The highest PL intensity is observed for x = 1.8–1.9 and annealing at 1100–1150 °C.[VII] Annealing at 1200 °C decreases the PL intensity. Similar decrease of the PL intensity was also observed for SiO_x ($1.05 < x < 1.75$) films prepared by MS.[84] Slightly different PL behavior is observed for SiO_x ($1.05 < x < 1.75$) films prepared by PECVD. For these samples, the PL intensity increases with the annealing temperature up to 1250 °C.[47,84]

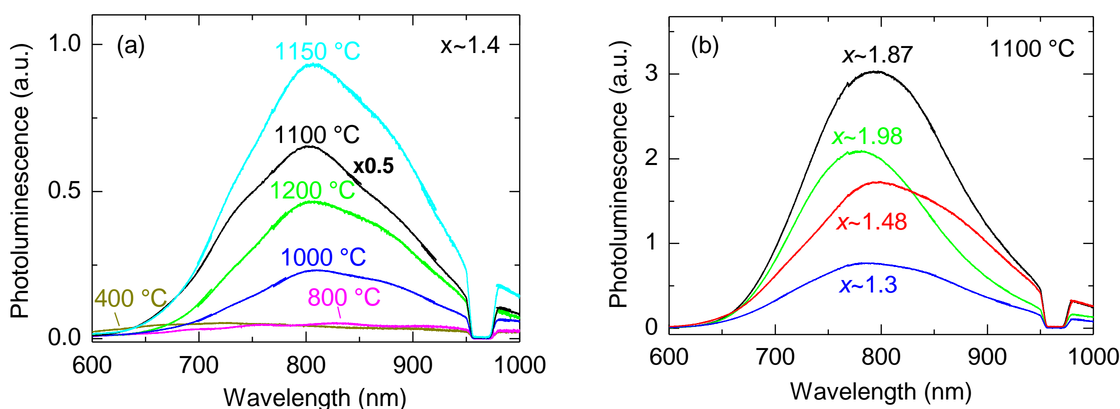

Figure 10 *Normalized PL spectra of (a) a $SiO_{1.4}$ film annealed at different temperatures and (b) SiO_x films prepared by MBD and annealed at 1100 °C. The hole in the spectra around 970 nm is due to the second order of the notch filter. Notice the multiplication factor in panel (a).*

The enhancement of the 1.5-eV PL by annealing at >1000 °C is accompanied by the formation of Si-nc detectable by Raman spectroscopy.[47,88,89,V,VII] This correlation seemingly suggests that the PL directly originates from these Si-nc. On the other hand, the PL intensity is strongest for samples with relatively small Si contents.[88,89] Moreover, for $x > 1.9$, no Si-nc and elemental Si are evidenced by the Raman and XPS data, respectively, whereas the PL is relatively strong (Figure 10b). In fact, the PL quantum yield steadily increases as the absorption coefficient and Si content decrease (Figure 11).[II,VII] These observations suggest that the Si-nc observed in the Raman spectra and detected by XPS as elemental Si are not direct light-emitting centers, which is in agreement with the defect origin of the PL.[45]

The PL position of our SiO_x films is relatively stable for different annealing temperatures (above 1000 °C) and Si contents (see Figure 10). These results seem to disagree with the studies of oxidized Si-nc prepared by MS.[32] Those experiments show that the PL position is size dependent for relatively large sizes (>3 nm) that are reliably measured by TEM. However, it is possible that the Si-nc sizes are similar for all our samples, which is in fact, indicated by the Raman spectra. Moreover, Wolkin et al.[22] have found that oxidation of Si-nc stabilizes the PL position for very small Si-nc (<3 nm). Thus, the stability of the PL position is also consistent with the hypothesis that the observed emission originates from very small Si grains (<3 nm). In general, one has to distinguish different types of Si-nc samples. For example, the experiments on hydrogen-passivated Si-nc show that the PL of Si-nc with diameters smaller than 3 nm should be below 600 nm, which is not the case for our samples. This difference in PL positions can be explained by the decrease of the bandgap upon passivation of Si-nc with oxygen.[77,125]

Now we discuss the different possibilities of assigning of the 1.5-eV PL to defects and/or very small Si grains. By analogy with oxidized p-Si,[22,31] the light-emitting centers can be the Si=O covalent bonds[44,88] or the bridge Si–O–Si bonds suggested by simulations.[76] Ultra-small (below ~1 nm) oxidized Si grains recently considered by theory is another candidate to explain the PL.[80] Several observations are consistent with the latter interpretation. First, the stable PL position for different Si content suggests small sizes (<3 nm).[22] The calculated band gaps of these Si clusters with diameters ~1 nm are 2–3 eV,[80] which agrees with the band gaps obtained for our samples (Figure 7).[V] The short PL lifetimes obtained for our samples (~1 μs)[II] also suggest that the PL originates from Si-nc that are quite smaller than

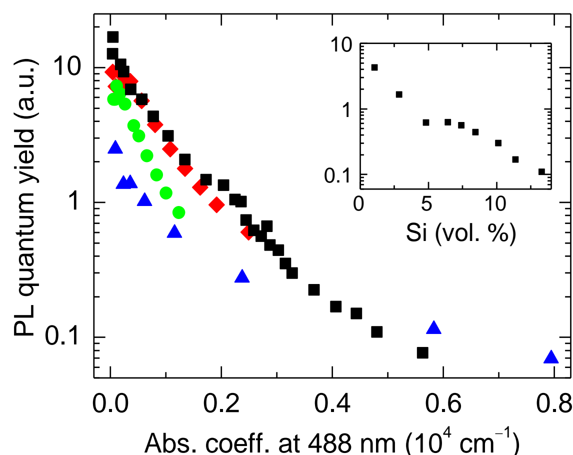

Figure 11 *Relative PL quantum yield for SiO_x prepared by MBD for annealing at 1000 °C (triangles), 1100 °C (squares), 1150 °C (diamonds), and 1200 °C (circles) as a function of the absorption coefficient at 488 nm. The insert shows the relative PL quantum yield as a function of the amount of elemental Si for annealing at 1100 °C.*

3 nm, for which the PL lifetime is ~40 μs.[126,VII] Moreover, the theoretical study by Luppi et al. reveals that Si-nc with sizes up to 1 nm in diameter with a Si–O–Si bridge bond at the surface emit at ~1.5 eV,[76] which is observed for our samples. The decrease of the PL after annealing at 1200 °C is reasonable if the amount of small optically active Si nanoclusters decreases at this temperature.

The direct excitation of the light-emitting centers by laser light is possible.[31] As another mechanism, laser light may be absorbed by relatively large Si clusters, and then the excitation is transferred to the light-emitting centers located at the Si-nc/SiO_2 interface[39,127] or in more disordered areas.[88,II] Non-radiative defects such as dangling bonds at the Si-nc/SiO_2 interface as well as defects inside and outside the Si-nc can efficiently trap the excitation and therefore quench the PL.[92] Annealing at ~1100 °C presumably decreases the amount of these non-radiative defects and/or intensifies the energy transfer to the radiative centers, which enhances the PL. The amount of the light-emitting centers may increase upon annealing; however, no direct evidence of this is available.

Kusova et al. have suggested that compressive stress on Si-nc in a silica matrix can redshift the PL.[128] Unfortunately, it is difficult to estimate stress on very small Si-nc using Raman spectroscopy, due to their low Raman scattering cross-section. Such small Si-nc can contribute to the broad low-frequency shoulder around 500 cm^{-1} (Figure 5). On the other hand, the observed Raman bands position at 518–519 cm^{-1} observed in our samples feature *unstressed* Si-nc with sizes of ~4 nm[116] that are also detected by TEM.[104] It can be speculated that no substantial stress is exerted also on smaller Si-nc.

3.1.3 Comparison of ion implantation and MBD (*x* ~ 1.8)

The structural and optical properties of as-prepared SiO_x materials deposited by MBD and ion implantation are very different.[V] It is found that amorphous clusters (>2 nm) are present in the as-grown MBD samples, as suggested by the broad Raman band at ~470 cm^{-1} (Figure 5) specific for amorphous Si[114] and high absorption (Figure 12a).[94] For the implanted samples annealed below 900 °C, the absence of Raman bands of Si and very low absorption (Figure 12a), suggests that only very small Si clusters (with sizes up to 1 nm) may be present.[94]

Upon annealing at 1000 °C, a narrow Raman band at about 516–517 cm^{-1} emerges for both types of samples, showing the formation of Si-nc. Compared with the as-prepared samples, the absorption coefficient increases for implantation but decreases for MBD (Figure 12b). After annealing at 1100–1200 °C, both types of samples become optically and structurally similar. For both types of samples, the Raman band is at ~518 cm^{-1} and the absorption coefficients are similar (Figure 12). These trends are reasonably explained by the growth and crystallization of Si clusters in the implanted sample and by the crystallization of the amorphous clusters in the MBD sample. Indeed, the absorption coefficient of crystalline Si is much smaller than that for amorphous Si. The higher absorption and normalized Raman intensity are observed after annealing (>1000 °C) for the MBD samples compared to the implanted sample (Figure 12), suggesting that the amount of Si-nc with sizes ≥2 nm is greater in the MBD samples. This conclusion is also supported

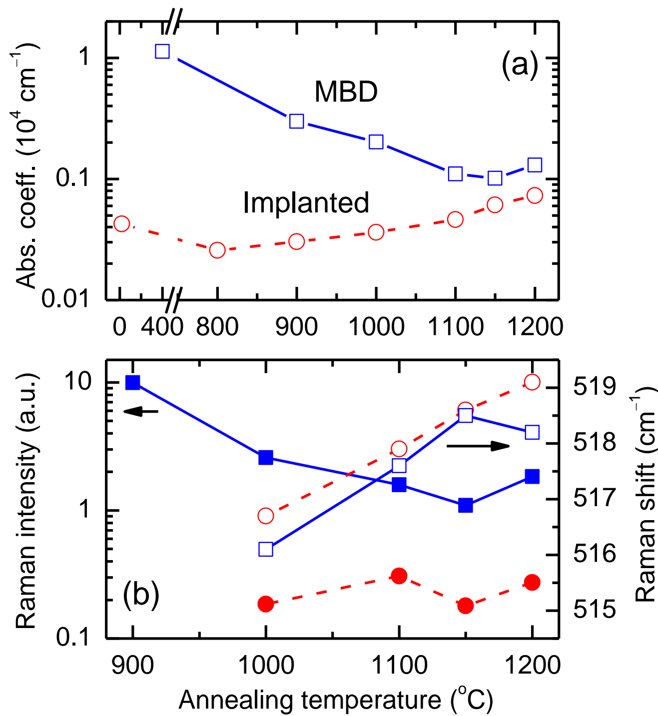

Figure 12 *(a) Absorption coefficient at 488 nm as a function of the annealing temperature for MBD (squares) and implanted (circles) samples and (b) normalized intensity (solid symbols) and position of the maximum (open symbols) of the Raman band.*

by the smaller band gap for the MBD sample (~2.6 eV) compared to that for the implanted sample (~3.3 eV).

When annealed below 900 °C, the PL with a maximum at about 650–700 nm is stronger for the implanted compared to the MBD sample (Figure 13), meaning larger amount of thermodynamically unstable radiative defects (see section 3.1.2) in the former.[49,83,122-124] For both preparation methods, annealing at ~1100 °C enhances the 1.5-eV PL that is slightly higher for the implanted sample (Figure 13), which is remarkable giving that the Raman intensity is smaller (Figure 12b). After annealing at 1200 °C, the PL decrease is especially pronounced for the implanted sample, which can originate from a thermal modification of the light-emitting centers, for example, an increase of the size of oxidized small Si grains.[80] In the case of the implanted sample, this conclusion is supported by the redshift of the PL

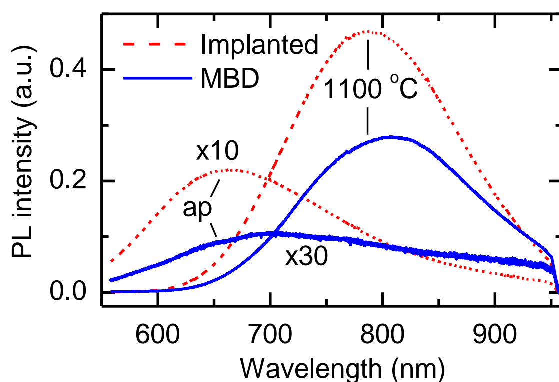

Figure 13 *PL spectra of as-prepared (ap) and annealed at 1100 °C $SiO_{1.8}$ films fabricated by MBD and Si ion implantation.*

to ~900 nm and decrease of the band gap from 3.3 to 2.8 eV for 1150 and 1200 °C, respectively.

For both types of samples even after annealing at 1200 °C, a large proportion of suboxides (~15%) is detected by XPS indicating that the Si–SiO_2 phase separation is not complete.

3.1.4 Laser heating of films on substrates

Relatively high laser-induced temperatures are found in SiO_x films on silica substrates under standard conditions of measurements.[VII] For example, laser power of ~130 mW focused to a 40-µm spot leads to a temperature of ~350 °C in a $SiO_{1.3}$ film annealed at 1100 °C (Figure 14a). The absorption coefficient of this film increases at 350 °C by ~40 % compared to the room temperature value, which is probably due to the thermally induced bang gap shrinking.[102] At this laser-induced temperature, the Raman band of Si-nc is observed at ~512.5 cm^{-1}, i.e. down-shifted by ~6 cm^{-1} from the room temperature position. The temperature dependence of the Raman shift is in excellent agreement with the calculations by Faraci et al. for Si-nc with sizes of 5 nm.[129] Similar temperature dependences were previously reported for crystalline Si and the free-standing $SiO_{1.7}$ film (see Figure 14a). The phonon confinement effect and residual stresses can explain the quantitative differences between the Raman band positions in these cases.

Figure 14b shows the laser-induced temperature for a free-standing $SiO_{1.7}$ film and SiO_x ($1.3 \leq x < 1.5$) film on silica substrate as a function of the laser power absorbed by a unit volume, which is proportional to $(1 - e^{\alpha d})P/d$, where P is the laser power, α is the absorption coefficient, and d is the film thickness.[100] The linear fit of the temperature versus

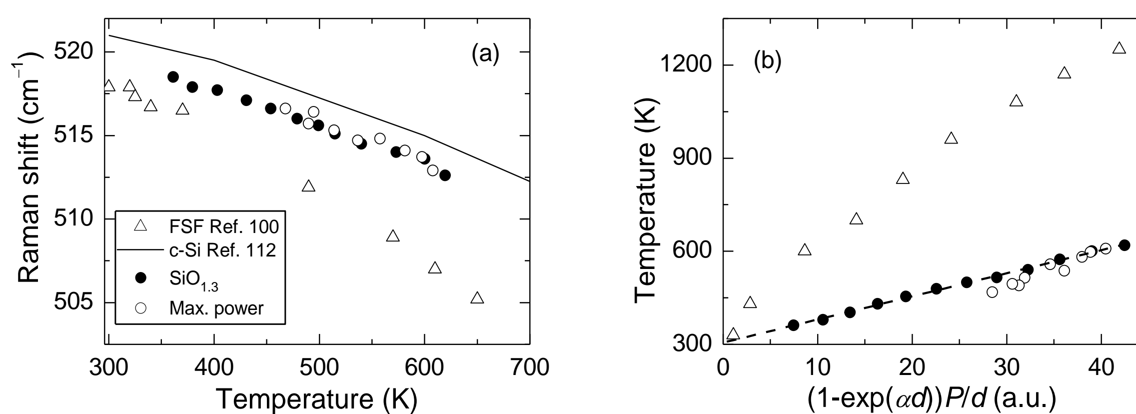

Figure 14 (a) *Raman shift as a function of the laser-induced temperature and (b) laser-induced temperature as a function of the laser power absorbed by a unit volume for $SiO_{1.3}$ annealed at 1100 °C at various 488 nm laser powers (solid circles) and for SiO_x ($1.3 < x < 1.5$) at the maximum laser intensity of ~10^4 W cm^{-2} (open circles). The data for a free-standing $SiO_{1.7}$ film[100] (FSF, triangles) and for crystalline Si[112] (solid line) are shown for comparison. The dashed line is a linear fit.*

the absorbed power yields the room temperature at zero power, which verifies the results. For the same absorbed power, the laser-induced temperature is larger in the free-standing film compared to the film on substrate, which is due to the thermal flow to the substrate in the latter case.

In Raman analysis of Si-nc, relatively high laser powers are often employed to obtain good signal-to-noise ratios. However, the laser heat, local stress, and the phonon confinement model are overlapping effects with respect to the Raman spectra. It follows that the laser-induced heat should always be carefully considered even for films on substrates (especially when using Raman microscopes) to obtain reliable information of the material structure.

3.2 Laser annealing of free-standing films

3.2.1 Laser-annealed areas

We studied cw laser annealing (488 nm) of free-standing SiO_x films (0.5 and 2 μm) and Si/SiO_2 SL (0.5 μm). Due to the preparation conditions (see section 2.1.1), the free-standing films contain small Si-nc up to 4 nm in diameter (see section 3.1.1).[100,104] The laser annealing for ~1 second was performed in air atmosphere. An optical photograph of a typical laser-annealed area on a free-standing film and a Raman map from the same area are presented in Figure 15. Three regions can be distinguished: central region, ring around the central region, and the pristine film outside the irradiated area.[IV,VI,VIII]

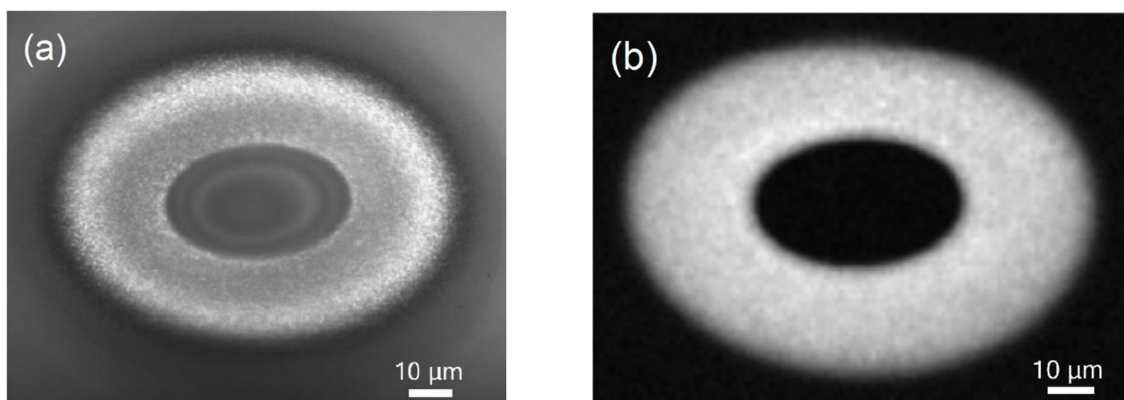

Figure 15 *(a) Optical microscope photograph and (b) Raman map of the Si-nc band. A 2-μm-thick free-standing* SiO_x *film was exposed to 488-nm light (~110 mW) through a lens (focus 150 mm). In the optical photograph, the sample was illuminated through the objective. The oval shape is due to a non-perpendicular direction of the laser beam. Lighter regions in the Raman map correspond to stronger Raman signals. The Raman signal was integrated in the 510–540* cm^{-1} *spectral range.*

Central region. The material in the central region is essentially amorphous SiO_2. For 0.5-µm-thick SiO_x (x ~ 1.7–1.8) films, this was directly shown by XPS and EELS methods.[IV] In accord, the TEM images and SAD patterns indicate a very homogeneous and amorphous structure of this region, and the FTIR spectra measured with high spatial resolution are similar to those of thermal silica. No Si-related peak is detected by Raman spectroscopy from the central region, the absorption is very low, and no PL is observed (Figure 16). In agreement, for 0.5-µm-thick Si/SiO_2 SL, no Si clusters are detected in BF-STEM images, EDS measurements indicate an increase of x in the central region compared to the pristine film.[VI,VIII] Quantitative analysis based on the EDS measurements is not possible because quantification using low-energy X-ray lines such as oxygen K alpha is not feasible. Small Si clusters (<1 nm) invisible by all employed microscopic methods are in principle possible in the central region. However, very small Si clusters are thermodynamically unfavorable,[130] and their formation seems to be improbable at high temperatures.[IV] Furthermore, these Si grains are presumably luminescent; however, practically no photoluminescence (at least by a factor of 100 compared to the pristine film) is detected from the central region.

Ring region. The EFTEM, BF-STEM, and TEM images show that the ring around the central region contains large Si-nc embedded in amorphous SiO_2 (Figure 17).[IV,VI,VIII] The maximum Si-nc sizes (~200 nm) for 0.5-µm-thick Si/SiO_2 SLs are on average two times larger than those detected for 0.5-µm-thick free-standing SiO_x films.[IV] This difference isreasonably explained by a larger Si content in Si/SiO_2 SLs (x ~ 0.7 from the deposition conditions) compared to SiO_x (x ~ 1.7–1.8) films. For 0.5-µm-thick Si/SiO_2 SL films, SEM, TEM, and AFM measurements detect several large holes (up to 200 nm) in the inner part of the ring region (Figure 17a,b). The crystallinity of the large Si clusters in the ring region is confirmed by the SAD measurements (for 0.5-µm-thick SiO_x) and Raman spectra. The Raman band is quite narrow and does not have a shoulder at 450–500 cm^{-1}, indicating the absence of amorphous phase and therefore efficient Si crystallization (see Figure 16a).

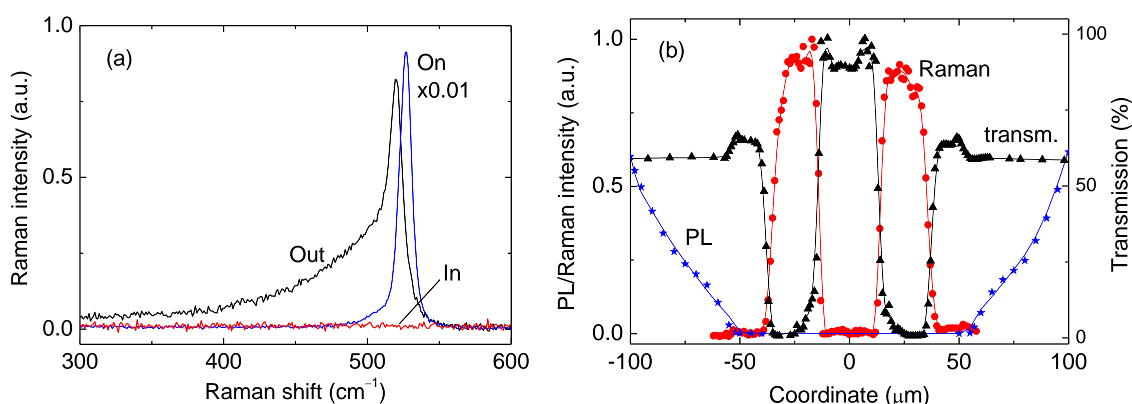

Figure 16 *(a) Raman spectra of a laser-annealed 2-µm-thick SiO_x (x ~ 1.7–1.8) film from regions in the center (in), on the ring (on), and outside the laser-annealed area (out). (b) Raman (circles), PL (stars), and transmission (triangles) cross-sections of the laser-annealed area. The cross-sections were measured in the vertical direction through the center of the laser-annealed area for the sample shown in Figure 15.*

The EELS spectra show the presence of Si and SiO_2 phases. In accord, FTIR spectra correspond to stoichiometric SiO_2 perturbed by Si–SiO_2 interface. The increase of the Raman by about 2–3 order of magnitude from this regions compared to the pristine film is explained by the resonance size effect for large Si-nc.[131,IV] The Raman bands from Si-nc in the ring region are typically shifted up to ~530 cm^{-1} (from the value of 521 cm^{-1} for crystalline Si) indicating a compressive stress on Si-nc. According to the mechanism proposed earlier, these large Si-nc are formed from the liquid phase, and the stress appears when their volume suddenly increased in the solid SiO_2 matrix.[95] Thus, the temperature in the ring region exceeds the melting point of Si (1685 K), and it must be even higher in the central region. Indeed, a temperature of ~2000 K was estimated by fitting the strong light-emission background upon irradiation with high laser intensities (~16 kW cm^{-2} at the sample).[99] The bright thermal radiation is also seen by the naked eye. High processing temperatures in the central region are also confirmed by the decrease of the film roughness detected by AFM.

These results demonstrate a Si–SiO_2 phase separation on a macroscopic scale: the central region (up to 30 μm) is cleaned of the Si excess, large Si-nc are formed and the Si excess is enhanced (found for 0.5-μm-thick SiO_x film by XPS and EELS) in the ring region. The macroscopic phase separation can be explained as follows. In the beginning of laser irradiation, the film structure is homogeneous so that the temperature gradient approximately corresponds to the intensity gradient in the Gaussian beam. The temperature gradient gives rise to a concentration gradient due to different diffusion properties of the mixture constituents.[IV] For example, Si, O, and SiO can diffuse in silica,[132] which changes the relative concentrations. Diffusion in temperature gradient is known as thermodiffusion or Ludwig-Storet effect.[133,134] As detected by EELS, XPS, and AFM measurements, the central region is typically thinner than the pristine film by about 30–40% and ~50% for 0.5-μm-thick Si/SiO_2 SL and SiO_x films, respectively. Moreover, AFM shows an increase of the film thickness in the ring region compared to the pristine film (see later in 3.2.3). These results are also indicative of macroscopic movement of Si from the central region.

3.2.2 Surface structure

Surface analysis (SEM and AFM) allowed us to discriminate Si-nc contacting the film surface in laser-annealed 0.5-μm-thick Si/SiO_2 SLs.[VI] These "surface Si-nc" have an unusual pear-like shape in the TEM images with the thinner part sticking out of the laser-illuminated surface. The AFM and SEM methods estimated that the thinner part above the surface (surface feature) has a spherical shape with a typical diameter of 60–70 nm, whereas the subsurface part is ~200 nm, as shown by TEM and BF-STEM images. Figure 17 shows this particle in TEM images with different magnifications.

The formation of the surface features was explained by the following mechanism. Since most of large Si-nc formed by laser annealing are under high compressive stress, it is possible that the laser-pressurized silicon can erupt from the film if it is separated from the ambient atmosphere by a very thin silica layer. The erupted Si is seen as the subparticle in Figure 17c. The volume of the subparticle (~70 nm in diameter) is ~5% of the volume of

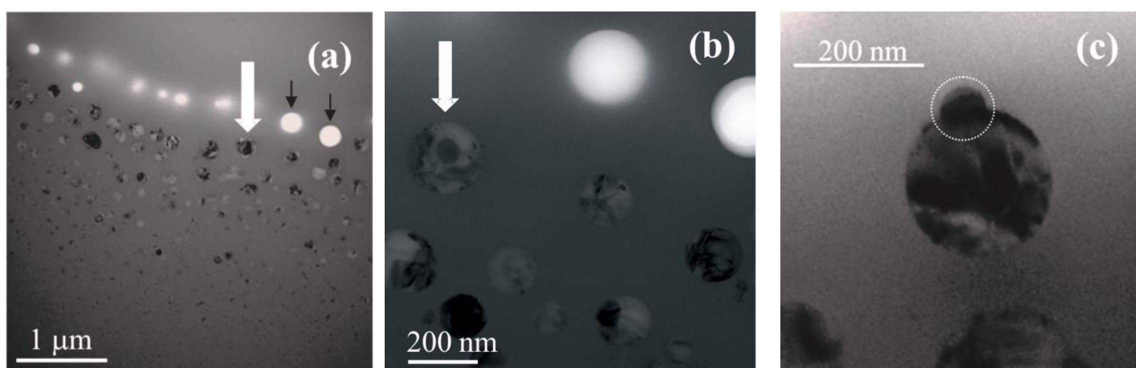

Figure 17 *TEM images of 0.5-μm-thick Si/SiO_2 SL film showing a Si particle located near the film surface (marked with white arrows). The images in panels a, b, and c are taken with different magnification. The bright spots are holes in the film; the holes observed in panel b are marked by black arrows in panel a, which were used as reference points. Panel c shows this particle in the tilted geometry, the surface subparticle being indicated by a dotted circle.*

the larger subsurface part of the nanocrystal (~200 nm in diameter). Eruption of this volume would lead to a substantial decrease of the compressive stress of the parent particle.[95] The fact that no eruptions are detected on the backside of the film seems to be consistent with this mechanism. Indeed, the temperature should be somewhat higher on the front side (laser-illuminated) of the film; hence, the covering silica film is softer at higher temperatures, which favours Si eruption on the front side of the film.

Raman measurements confirm the proposed eruption model. Spot 1 in Figure 18a marks the position of a surface Si nanocrystal in the Raman map of Si-nc. The same surface Si

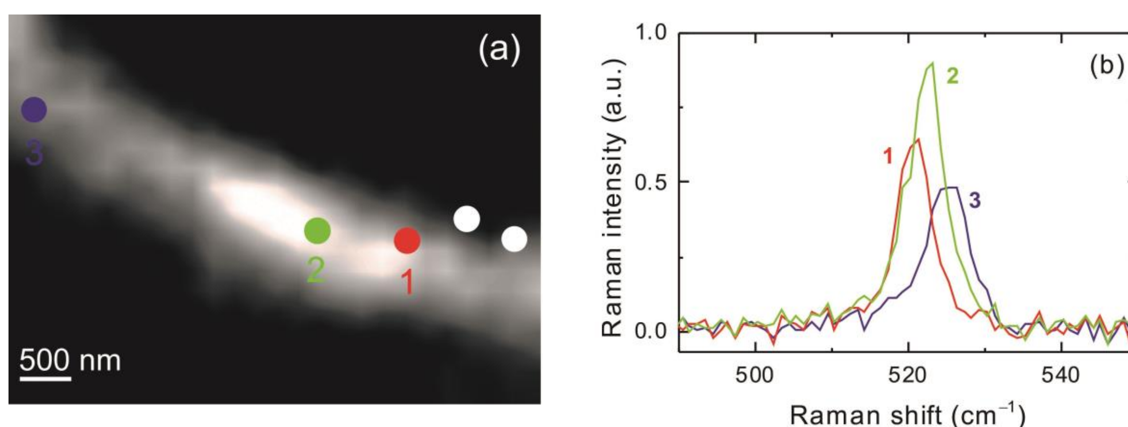

Figure 18 *Raman characterisation of the region shown in Figure 17a. (a) Raman map of Si-nc (integration from 515 to 530 cm^{-1}) obtained with a 100× objective and steps of 0.2 μm. The white circles show positions of two holes used for the positioning. (b) Raman spectra obtained in positions 1, 2, and 3 shown in panel a. Position 1 corresponds to the surface Si nanocrystal shown in Figure 17.*

nanocrystal is shown in the TEM images (Figure 17). The Raman shift of ~520 cm^{-1} obtained in this position (spectrum 1, Figure 18b) indicates a low stress. It is reasonable that Si eruption can relax stress also around surface Si-nc. Indeed, the compressive stress is partially relaxed at a distance of about 1 μm from the surface feature (spectrum 2).

3.2.3 Effect of the annealing atmosphere

The studies described above were performed in air atmosphere (containing ~20% of oxygen), which can cause some oxidation of Si during laser annealing. Indeed, oxygen can diffuse through the film oxide to Si-nc.[135-137] This may decrease the excess of Si, especially in the central region, where the temperatures are the highest. To evaluate this effect, we compared laser annealing in atmospheres containing different amounts of oxygen (Ar, N_2, O_2, and air atmospheres). This was done in detail for 0.5-μm-thick Si/SiO_2 SL and 1-s exposure.[VIII]

Central region. For all annealing atmospheres, the center of laser-annealed areas most probably consists of amorphous silica without Si excess. This is indicated by the absence of the Raman signal of Si-nc in this area, an increase of *x* compared to the pristine film detected

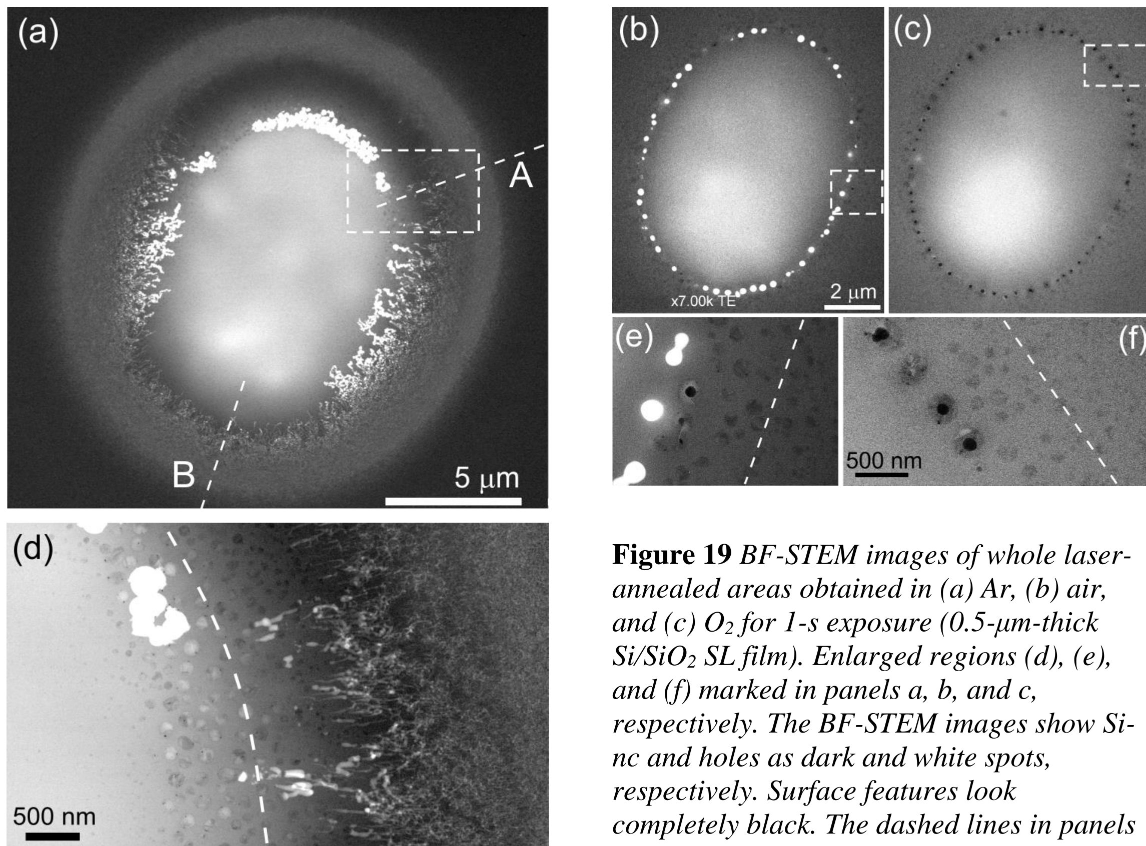

Figure 19 *BF-STEM images of whole laser-annealed areas obtained in (a) Ar, (b) air, and (c) O_2 for 1-s exposure (0.5-μm-thick Si/SiO_2 SL film). Enlarged regions (d), (e), and (f) marked in panels a, b, and c, respectively. The BF-STEM images show Si-nc and holes as dark and white spots, respectively. Surface features look completely black. The dashed lines in panels d, e, and f indicate the position of the maximum Raman signal. The scale is the same in panels a, b, c and in d, e, f.*

by EDS, and by the absence of Si clusters in BF-STEM images (see Figure 19). Large Si-nc (up to 150–300 nm) are formed in the ring regions, and the film thickness tends to increase compared to that of the pristine film. The change of the film thickness was estimated using the AFM images taken from both sides of the film (Figure 20). These results support the concept of macroscopic Si–SiO_2 phase separation as a result of laser annealing.

The effect of oxygen in the laser annealing process can be analyzed by comparing the film thickness in the central region obtained for different atmospheres. Indeed, two competitive processes, thermodiffusion and Si oxidation, affect the film thickness in the opposite directions, tending, respectively, to decrease and to increase it. For Ar atmospheres, the central region is thinner by ~150 nm than the pristine film, i.e. the thickness is about 350 nm. This observation supports the concept of the macroscopic phase separation because Si oxidation does not operate in the inert atmospheres. A similar change of the thickness occurs in air (the thickness of the central region is 300–350 nm) indicating minor Si oxidation also in this case. In contrast, laser annealing in pure O_2 increases the film thickness in the central region by ~20 nm compared to the pristine film. Thus, both thermodiffusion and Si oxidation seem to operate in this case, practically compensating each other.

A large part of Si can be in principle oxidized under our experimental conditions. The difference between the film thickness of the central region for inert and O_2 atmospheres is ~200 nm. 200 nm of SiO_2 can be formed by oxidation of about 100-nm Si layer, which corresponds to ~40% of all amount of Si in the pristine SL (from the deposition conditions,

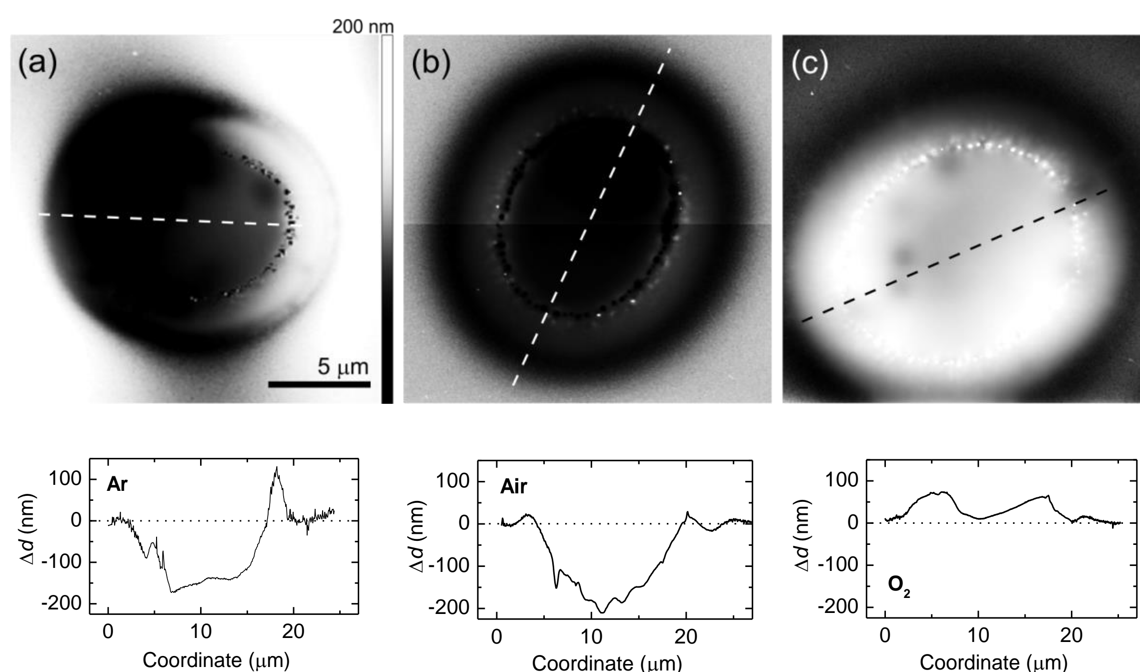

Figure 20 *AFM of the front side of laser-annealed areas for 1-s exposure. Tapping mode images and the change of the film thickness Δd from the value for the pristine film (500 nm) in cross-sections shown by dashed lines for laser-annealed areas obtained in (a) Ar, (b) air, and (c) O_2 atmospheres. The scale is the same in all tapping mode images.*

the total thickness of the 125 Si layers is ~250 nm). On the other hand, according to the model suggested by Deal and Grove for crystalline Si, 1 bar of dry O_2 at 1200 °C produces ~20-nm oxide film during 1 s, whereas a ~33-nm oxide is formed for 100 s.[136] It should be reminded that the temperature of laser annealing is sufficiently higher.[99] Of course, these estimates should be considered with caution, first of all, because our pristine material is very different from crystalline Si.

Si-nc and holes in the ring region. The amount of O_2 in the ambient atmosphere during laser annealing has a strong effect also on the structure of the ring region with large Si-nc. For inert atmospheres, the AFM and BF-STEM images show that the ring region is very inhomogeneous (see Figure 19 and Figure 20a). It contains sections with large Si-nc up to 150 nm in diameter (Figure 19d), with large non-spherical holes up to 300 nm, and with smaller Si-nc up to 50 nm in diameter (in the area around line *B* in Figure 19a). No surface Si-nc are observed on the both front and back sides of the film (as confirmed by AFM and SEM). Raman spectroscopy indicates Si-nc with different stresses (Raman shifts 518–530 cm^{-1}) and regions with different intensities of Raman bands of Si-nc. BF-STEM images show a "belt" of nano-channels (or pores) around the ring region (see Figure 19a and the right side of Figure 19d). The size of these nano-channels can be as low as a few to tens of nanometers. For pure O_2 atmosphere, besides Si-nc inside the film, SEM and AFM of the front side of the film clearly show a regular chain of large surface Si-nc at the inner part of the ring (Figure 19c,f; Figure 21b). These surface Si-nc can be up to 300 nm in diameter. In agreement with the suggested eruption model, Raman spectroscopy shows a relaxed stress around the chain of the surface Si-nc (Raman shifts of ~520 cm^{-1}), whereas the Si-nc at the outer part are still under compressive stress. No holes are present in the laser-annealed areas produced in O_2 atmosphere.

Remarkably, for annealing in air, a chain of holes is present at the inner part of the

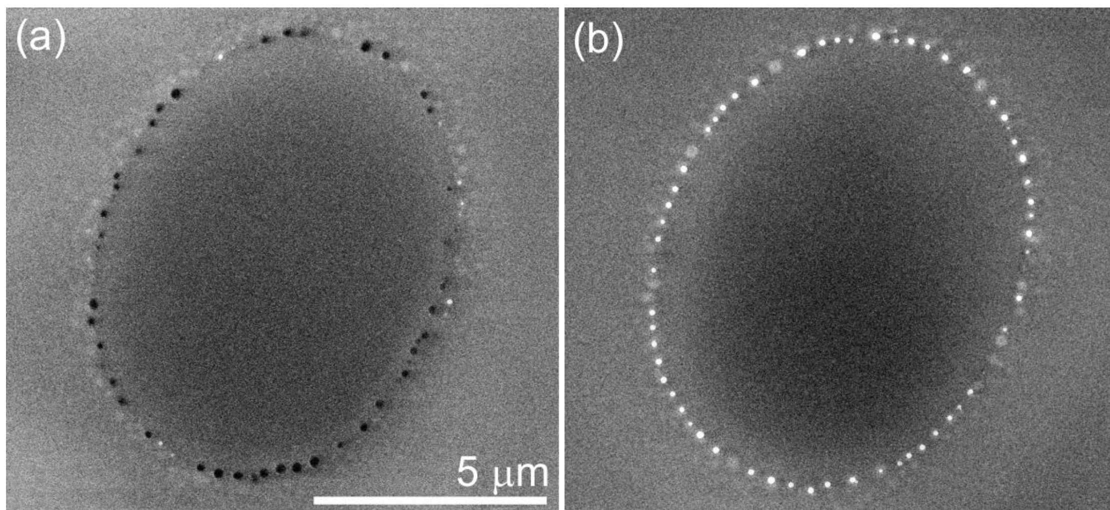

Figure 21 *SE images of the front side of laser-annealed areas produced in (a) air and (b) O_2 atmospheres during 1-s exposure. Surface features are white, holes are black. The scale is the same in both panels.*

Si-nc ring, where, for O_2 atmosphere, a chain of large surface Si-nc is located (see Figure 19 and Figure 21). Thus, it can be suggested that the holes in the laser-annealed areas are formed at the positions of surface Si-nc removed from the film and the eruption mechanism may operate to some extent. The laser-annealed areas with larger number of holes contain less surface Si-nc, and the presence of oxygen increases the amount of surface Si-nc. This suggests that oxygen decreases the removal of Si particles by the formation of a thin oxide layer covering surface Si-nc, which "glues" them to the film. The large irregular holes obtained in the inert atmospheres also presumably originate from the Si-nc removed from the film. The suggested mechanism of the formation of holes is consistent with the dependence of the maximum Si-nc sizes on the annealing atmosphere. For inert atmospheres, the maximum diameters of Si-nc visible in BF-STEM images are only ~150 nm because larger Si-nc are removed from the films forming holes up to 300 nm. For O_2 atmosphere, the largest Si-nc (up to 300 nm) are detected because they are well protected by thin oxide layers. Annealing in air represents an intermediate case where the largest Si-nc are ~200 nm, and some Si-nc are removed forming holes.

Holes in the ring regions are observed only for 0.5-µm-thick Si/SiO_2 SLs, and they are absent for 0.5-µm-thick SiO_x ($x \sim 1.7$–1.8) films laser-annealed in air in similar conditions. In the latter case, the Si-nc have sizes up to 100 nm. In this situation, most of the Si-nc are probably located below the film surface and, therefore, cannot be removed to form holes.

Secondary Si depletion. The model of macroscopic phase separation finds additional support from the observation of secondary Si depletion outside the ring region.[VIII] Figure 22 shows Raman cross-sections measured through characteristic ring regions of the laser-annealed areas prepared in inert (Ar) and O_2 atmospheres. The coordinate $x = 0$ approximately corresponds to the maximum Raman signal in the ring regions (see also

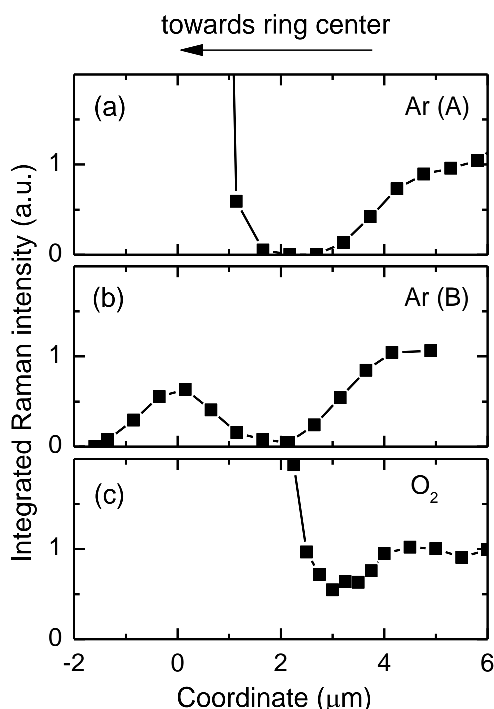

Figure 22 *Characteristic Raman cross-sections (a) and (b) along the dotted lines marked in panel a Figure 19 as A and B, respectively, (c) through typical ring region for O_2. For air, the cross-section is similar to that obtained for O_2. The Raman signal was integrated in the 230–585 cm^{-1} range. The normalizing factor corresponds to the Raman intensity measured from the pristine film.*

dashed lines in Figure 19d-f). It has been found that for 488-nm laser light, the Raman enhancement is the strongest for spherical Si particles with diameters of ~112.5 nm.[131] In agreement, Si-nc with sizes ~100 nm are observed in the areas with the strongest Raman signal (Figure 19d-f). At coordinates >5 μm (Figure 22), the Raman spectra are similar to that from the pristine film. The Raman intensity is relatively weak in region *B* for Ar atmosphere because the Si-nc sizes are smaller than ~50 nm, as estimated from BF-STEM images, i.e. smaller than the resonance value of ~112.5 nm.[131]

For inert atmospheres, there is a spatial interval (1–1.5 μm wide) located at coordinates 2–3 μm, where the Raman signal is at least 10 times lower compared to the pristine film, i.e. practically absent (Figure 22). For air and O_2, this decrease of Raman intensity is less pronounced, but still observable. In the attempt to explain the formation of this interval with low Raman intensity, we speculate that after the large Si-nc are formed in the ring region during laser annealing, the absorption coefficient in this area strongly increases resulting in an increase of the temperature. Due to the thermal conductivity, the temperature of the vicinity also increases, which leads to a temperature gradient and additional macroscopic phase separation outside the ring region. This process seems to be more efficient for the inert compared to oxygen-containing atmospheres. The position of this spatial interval roughly coincides with the position of the belt of nano-pores and nano-channels observed by SEM. The exact mechanism of the formation of these pores is unclear.

3.2.4 Effect of the exposure duration

Laser annealing at different exposures (10 ms and 100 s in addition to 1 s) were studied for 0.5-μm-thick Si/SiO_2 SL mostly in air atmosphere.[VIII] For all exposures (10 ms – 100 s), EDS and Raman measurements of the central region yield similar results (an increase of x and no Raman signal from Si-nc relative to the pristine film) and no Si clusters are visible in the BF-STEM images (Figure 23). Thus, 10-ms exposure is enough for the substantial removal of the Si excess from the central region. In other words, these data show that this process essentially occurs at a millisecond time scale.

However, the ring regions differ for different exposures. For 10-ms exposures, no holes or surface features are detected. The growth of Si-nc in the ring is not finished. The Si-nc have relatively small sizes. For 10-ms exposure in air, Si-nc up to 20–30 nm are detected by SEM (see Figure 23d). For 1-s and 100-s laser exposures, the Si-nc can reach up to 200 and 250 nm in diameter, respectively (Figure 23e,f). Thus, the increase of the laser-annealing duration increases the Si-nc size. Evidently, coalescence of Si-nc can be suggested, based on the fact that their amount decreases (compare Figure 23e and 23f).[50] The increase of Si-nc sizes with the exposure duration probably can explain the greater amount of surface Si-nc after 100-s annealing compared to 1-s annealing (compare Figure 23b and 23c). For other atmospheres, the prolonged laser annealing (100 s) also decreases the amount of small Si-nc and increases the average sizes of Si-nc compared to exposures for 1 s. The Si-nc sizes for 10-ms exposures (20–30 nm) are below the resonance value of ~112.5 nm. This explains why no Raman enhancement is observed from these small Si-nc (compare the Raman spectra for 10 ms and for the pristine film in Figure 24).

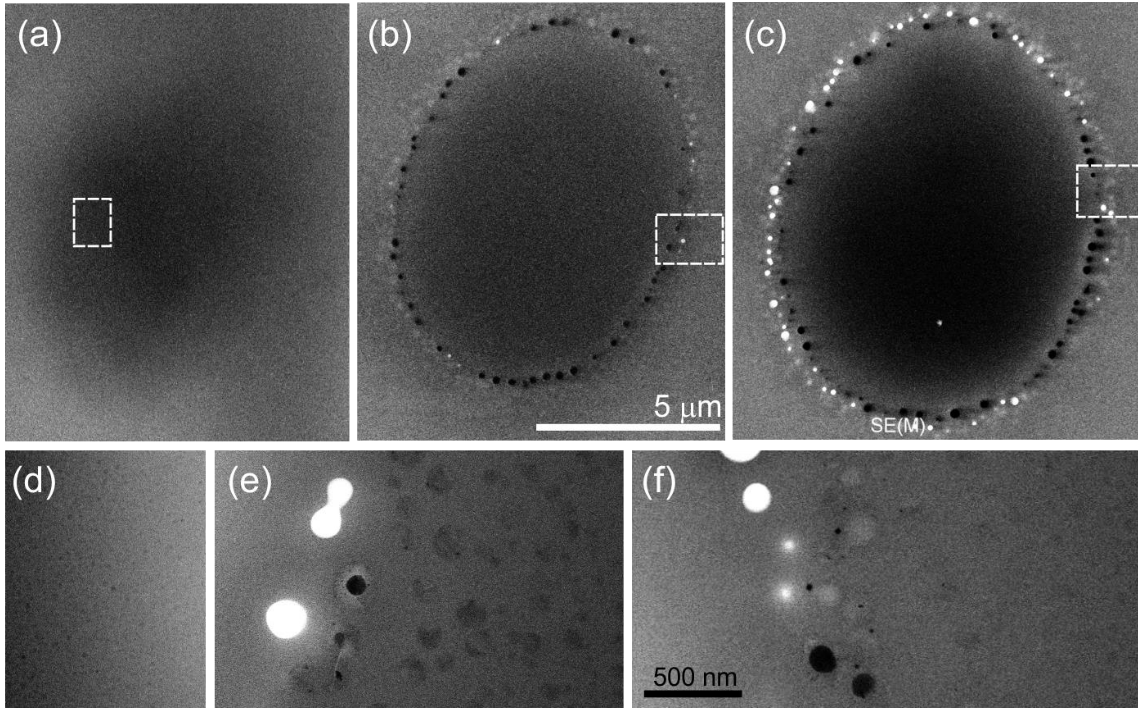

Figure 23 *Effect of the laser exposure duration for 0.5-µm-thick Si/SiO$_2$ SL. SE images of whole laser-annealed areas obtained by laser annealing in air for (a) 10 ms, (b) 1 s, and (c) 100 s. BF-STEM images (d), (e), and (f) of rectangular regions marked in panels a, b, and c, respectively. The SE images show surface features and holes in the film as bright and dark spots, respectively. The BF-STEM images show Si-nc and holes as dark and bright spots, respectively. The scale is the same in panels a, b, c and in d, e, f.*

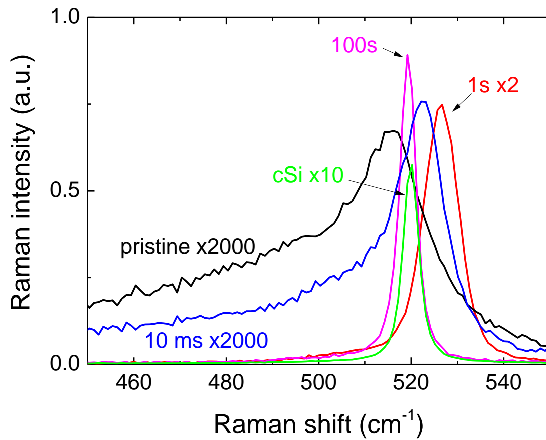

Figure 24 *Typical Raman spectra from the ring region of laser-annealed areas on 0.5-µm-thick Si/SiO$_2$ SL prepared by 10 ms, 1 s, and 100 s exposures in air as well as from the pristine film and crystalline Si wafer (c-Si).*

The small Raman signal from the ring regions (for 10 ms exposures) can be also connected with an increase of reflection and with interference effects. In contrast, for 1-s and 100-s exposures, the Raman signal is enhanced by 2–3 orders of magnitude compared to that from the pristine film. The Raman band for 10-ms exposure has a smaller low-frequency shoulder compared to the pristine film, meaning that the amount of disordered Si and/or small Si clusters is reduced. When the exposure increases from 10 ms to 100 s, the Raman band further narrows indicating that the amount of disordered Si further decreases. For 100-s exposure, the width of the Si-nc Raman band becomes as narrow as that from crystalline Si wafer, which indicates an almost perfect crystalline structure.

Similarly to 1-s exposure, for 10-ms annealing, the Si-nc in the ring region are formed from the melt phase because they are under compressive stress as shown by Raman shifts of ~525 cm^{-1}. On the contrary, no stress on Si-nc is detected for 100-s exposures for all studied annealing atmospheres (Raman shift ~518 cm^{-1}). This fact may show that for the long exposure, the temperature of large Si-nc is below the melting point. The decrease of the temperature for long exposure may be explained by the decrease of the absorption when the Si-nc become much larger than the resonance size of ~112 nm (for 488 nm light).[131] As other possibilities, the silica matrix can soften at long laser exposures. Our present data are insufficient to distinguish these mechanisms.

3.2.5 Optical memory

In this section, we describe two concepts of optical memory based on crystallization of Si nanostructures in free-standing Si/SiO_2 SL films by a strongly focused laser beam.[III] The first concept is based on the Raman signal enhancement and the second one uses the silicon stress.

The concept of Raman enhancement. The free-standing film is irradiated by a strongly focused laser beam (488 nm) using a ×100 objective during 10 ms – 1 s, which produces laser spots with sizes below 1 μm. The laser spots are clearly visible in camera photographs, which indicates a change in the reflection coefficient of the film. Three such spots are shown in optical photograph in Figure 25a. Raman, PL, and transmission profiles through a typical laser-annealed spot are presented in Figure 25b. The Raman signal is strongly enhanced whereas transmission is decreased due to temperature-induced Si–SiO_2 phase separation, ordering and growth of Si-nc, and the resonance size effect.[95,99,100,131,IV]

The observed laser crystallization is a case of non-volatile memory. Binary digits can take values of either 0 or 1 as demonstrated in Figure 25c. The smaller Raman intensity corresponds to 0, whereas the higher Raman intensity represents 1. Similar data reading can be obtained by transmission or reflection measurements. The data pixels occupy a typical space of ~1 μm. The estimated data density for this method is ~1 bit/μm^2, which can be improved by using stronger objectives and shorter laser wavelength. The nature of the used material provides high thermal stability of the described optical memory.

The thermal stability of the laser-crystallized spots was tested by furnace annealing for 1 hour at 1200°C in nitrogen atmosphere. As expected, Raman and transmission signals remained unchanged. This approach does not allow erasing and rewriting information.

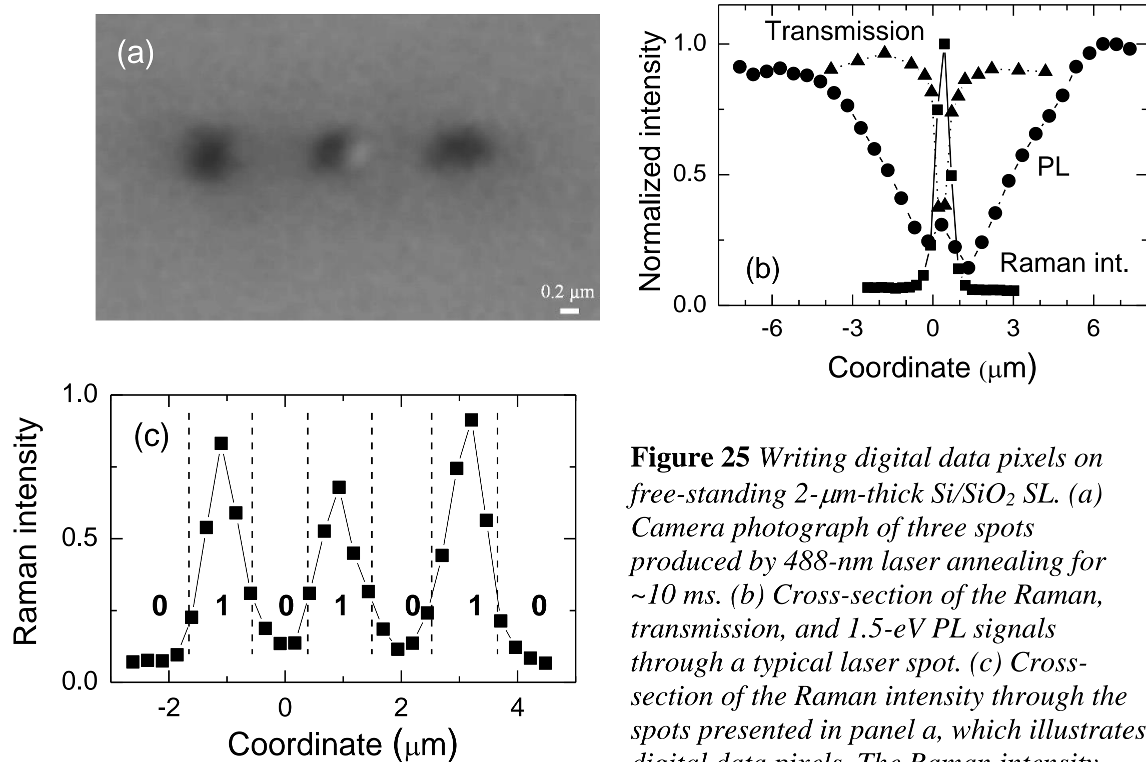

Figure 25 *Writing digital data pixels on free-standing 2-μm-thick Si/SiO2 SL. (a) Camera photograph of three spots produced by 488-nm laser annealing for ~10 ms. (b) Cross-section of the Raman, transmission, and 1.5-eV PL signals through a typical laser spot. (c) Cross-section of the Raman intensity through the spots presented in panel a, which illustrates digital data pixels. The Raman intensity was integrated in the 500–540 cm^{-1} region.*

The concept of Si-nc stress. First, a free-standing Si/SiO_2 SL film is shortly irradiated with a relatively large laser spot (10–40 μm in diameter), which produces an extended area (similar to the spot shown in Figure 15a) with a compressive stress of ~3 GPa. This stress is evidenced by Raman bands at ~527 cm^{-1} (Figure 26a).[95,101] Next, the stressed area is irradiated by a highly focused laser beam using a 100× objective and reduced laser power (<10 mW). As a result of the laser annealing below the Si melting temperature, the stress is released in the irradiated spot and the Raman band shifts down to ~518 cm^{-1}. The typical size of the spot with relaxed stress is ~1 μm (Figure 26b). The transmission is practically unchanged upon the stress relaxation, and this spot is invisible in camera photographs. The laser-induced decrease in the Raman shift from 527 cm^{-1} writes data pixels on the film similarly to the concept based on the Raman enhancement. The data can be erased by inducing stress by a broad high-power laser beam and re-written again.[95,101] The retention time of the stress-based memory is estimated to be about 1 year at ~300 °C.[95]

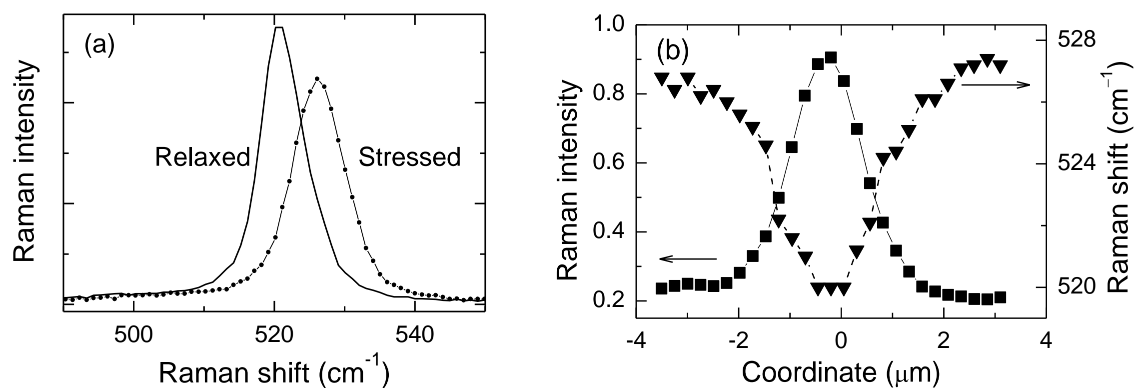

Figure 26 (a) *Raman spectra of Si-nc with stress of ~3 GPa and after laser-induced relaxation (for 2-μm-thick Si/SiO$_2$ SL). (b) Cross-sections of the Raman band position and the Raman intensity integrated in the 510–520 cm^{-1} region.*

4. Conclusions in brief

This work is focused on optical and structural properties of Si-nc in SiO_x ($x < 2$) and Si/SiO_2 SL films. The SiO_x films have different Si contents and annealed at different temperatures up to 1200 °C.

For different Si contents in SiO_x films, the Si-nc Raman signal and the absorption coefficient are proportional to the amount of elemental Si detected by XPS. On the other hand, the Raman scattering cross-section of elemental Si is about three times lower compared to that of crystalline Si. This difference can be explained by the presence of small Si-nc (<2 nm) and/or by the different properties of bulk and nanoscale Si.

The measured optical properties of SiO_x films are compared with the values estimated by using the effective medium approximation and XPS results. A good agreement is found between the measured and calculated refractive index. The results for absorption suggest high transparency of nanoscale suboxide. The extinction coefficient for elemental Si is found to be between the values for crystalline and amorphous Si. Thermal annealing increases the degree of Si crystallization; however, the Si–SiO_2 phase separation is not complete after annealing at 1200 °C.

The PL quantum yield increases as the amount of elemental Si decreases. It follows that the 1.5-eV PL from the SiO_x films annealed above 1000 °C is probably not directly from Si-nc responsible for absorption and detected by Raman spectroscopy. According to these results, the light-emitting centers may be small (~1 nm) oxidized Si grains or oxygen-related defects, which are not detectable by Raman spectroscopy.

The as-prepared SiO_x films deposited by MBD and ion implantation are structurally and optically very different. Large amorphous clusters (>2 nm) are present in the MBD films whereas they are absent in the implanted samples as suggested by absorption and Raman spectroscopy. After annealing at ~1100 °C the samples become similar and possess comparable amounts of Si-nc.

Laser-induced thermal effects are found for SiO_x films on substrates illuminated by focused laser light. In our experiments, a temperature of ~350 °C was measured for SiO_x (x ~ 1.3) films on silica substrate for laser intensity of 10^4 W cm^{-2}, which down-shifts the Raman band by ~6 cm^{-1}. This effect should be taken into account in optical measurements using focused laser beams.

Cw laser irradiation can produce very high temperatures in free-standing SiO_x and Si/SiO_2 films, which changes their structure and optical properties. The center of a laser-annealed area is very transparent and consists of amorphous SiO_2 with possible (but not probable) inclusions of ultra-small Si grains (<1 nm). Large Si-nc (up to 300 nm) are observed in the ring around the central region. These Si-nc produce high absorption and they are typically under compressive stress, which is connected with the crystallization from the melt phase. Some of the large Si-nc exhibit surface features, which is interpreted in terms of eruption of pressurized Si from the film. Some of these "surface" Si-nc are removed from the film forming holes of similar sizes. The presence of oxygen in the laser-annealing atmosphere decreases the amount of removed Si particles most probably due to oxidation of their surface.

The structure of laser-annealed areas is explained by thermodiffusion in temperature gradient, which suggests the macroscopic Si–SiO_2 phase separation. Comparison of the structure of central regions for laser annealing in oxygen, air, and inert atmospheres excludes the dominating effect of Si oxidation, thus supporting the mechanism of macroscopic Si–SiO_2 phase separation.

By using a strongly focused laser beam, the structural changes in the free-standing films can be obtained in areas of submicron sizes. A concept of high-density nonvolatile optical memory with superior thermal stability is suggested, where the information can be read, rewritten and erased by optical means.

References

1 *Silicon Nanophotonics: Basic Principles, Present Status and Perspectives*, edited by L. Khriachtchev (Pan Stanford, Singapore, 2008).

2 *Silicon Photonics II: Components and Integration*, edited by D. J. Lockwood and L. Pavesi (Springer-Verlag Berlin, Germany, 2011).

3 *Nanostructures in Electronics and Photonics*, edited by F. Rahman (Pan Stanford, Singapore, 2008).

4 *Photonics: Optical Electronics in Modern Communications*, edited by A. Yariv and P. Yeh (Oxford University Press, Incorporated, 2007).

5 B. Jalali and S. Fathpour, J. Lightwave Technol. 24, 4600 (2006).

6 R. Soref, IEEE J. Sel. Top. Quant. Electron. 12, 1678 (2006).

7 N. Daldosso and L. Pavesi, Laser Photonics Rev. 3, 508 (2009).

8 *Front Matter, in Silicon Photonics: The State of the Art*, edited by G. T. Reed (John Wiley & Sons, Ltd, Chichester, UK, 2008).

9 L. Pavesi, J. Phys. Cond. Matt. 15, R1169 (2003).

10 D. J. Lockwood, NATO Asi Ser., Ser. E 348, 185 (1998).

11 D. J. Lockwood and L. Pavesi, Top. Appl. Phys. 94, 1 (2004).

12 B. Delley and E. F. Steigmeier, Phys. Rev. B 47, 1397 (1993).

13 S. Ogut, J. R. Chelikowsky, and S. G. Louie, Phys. Rev. Lett. 79, 1770 (1997).

14 P. A. Wolff, J. Phys. Chem. Solids 16, 184 (1960).

15 L. T. Canham, Appl. Phys. Lett. 57, 1046 (1990).

16 A. G. Cullis and L. T. Canham, Nature 353, 335 (1991).

17 S. Gardelis, J. S. Rimmer, P. Dawson, B. Hamilton, R. A. Kubiak, T. E. Whall, and E. H. C. Parker, Appl. Phys. Lett. 59, 2118 (1991).

18 A. Bsiesy, J. C. Vial, F. Gaspard, R. Herino, M. Ligeon, F. Muller, R. Romestain, A. Wasiela, A. Halimaoui, and G. Bomchil, Surf. Sci. 254, 195 (1991).

19 C. Delerue, G. Allan, and M. Lannoo, Phys. Rev. B 48, 11024 (1993).

20 S. M. Prokes, Appl. Phys. Lett. 62, 3244 (1993).

21 J. L. Gole, F. P. Dudel, D. Grantier, and D. A. Dixon, Phys. Rev. B 56, 2137 (1997).

22 M. V. Wolkin, J. Jorne, P. M. Fauchet, G. Allan, and C. Delerue, Phys. Rev. Lett. 82, 197 (1999).

23 G. Ledoux, J. Gong, F. Huisken, O. Guillois, and C. Reynaud, Appl. Phys. Lett. 80, 4834 (2002).

24 D. C. Hannah, J. H. Yang, P. Podsiadlo, M. K. Y. Chan, A. Demortiere, D. J. Gosztola, V. B. Prakapenka, G. C. Schatz, U. Kortshagen, and R. D. Schaller, Nano Lett. 12, 4200 (2012).

25 T. Y. Kim, N. M. Park, K. H. Kim, G. Y. Sung, Y. W. Ok, T. Y. Seong, and C. J. Choi, Appl. Phys. Lett. 85, 5355 (2004).

26 B. Rezgui, A. Sibai, T. Nychyporuk, M. Lemiti, and G. Bremond, J. Lumin. 129, 1744 (2009).

27 L. Pavesi, L. Dal Negro, C. Mazzoleni, G. Franzo, and F. Priolo, Nature 408, 440 (2000).

28 L. Khriachtchev, M. Räsänen, S. Novikov, and J. Sinkkonen, Appl. Phys. Lett. 79, 1249 (2001).

29 N. Koshida and H. Koyama, Appl. Phys. Lett. 60, 347 (1992).

30 G. Franzo, A. Irrera, E. C. Moreira, M. Miritello, F. Iacona, D. Sanfilippo, G. Di Stefano, P. G. Fallica, and F. Priolo, Appl. Phys. A 74, 1 (2002).

31 F. L. Zhou and J. D. Head, J. Phys. Chem. B 104, 9981 (2000).

32 S. Takeoka, M. Fujii, and S. Hayashi, Phys. Rev. B 62, 16820 (2000).

33 D. Nesheva, C. Raptis, A. Perakis, I. Bineva, Z. Aneva, Z. Levi, S. Alexandrova, and H. Hofmeister, J. Appl. Phys. 92, 4678 (2002).

34 E. Lioudakis, A. Othonos, G. C. Hadjisavvas, P. C. Kelires, and A. G. Nassiopoulou, Physica E 38, 128 (2007).

35 C. Garcia, B. Garrido, P. Pellegrino, R. Ferre, J. A. Moreno, J. R. Morante, L. Pavesi, and M. Cazzanelli, Appl. Phys. Lett. 82, 1595 (2003).

36 Y. Kanemitsu, T. Ogawa, K. Shiraishi, and K. Takeda, Phys. Rev. B 48, 4883 (1993).

37 C. Ternon, C. Dufour, F. Gourbilleau, and R. Rizk, Eur. Phys. J. B 41, 325 (2004).

38 B. G. Fernandez, M. Lopez, C. Garcia, A. Perez-Rodriguez, J. R. Morante, C. Bonafos, M. Carrada, and A. Claverie, J. Appl. Phys. 91, 798 (2002).

39 Y. Kanemitsu, H. Uto, Y. Masumoto, T. Matsumoto, T. Futagi, and H. Mimura, Phys. Rev. B 48, 2827 (1993).

40 K. S. Zhuravlev, A. M. Gilinsky, and A. Y. Kobitsky, Appl. Phys. Lett. 73, 2962 (1998).

41 C. S. Garoufalis and A. D. Zdetsis, Phys. Chem. Chem. Phys. 8, 808 (2006).

42 K. Dohnalova, K. Kusova, and I. Pelant, Appl. Phys. Lett. 94, 211903 (2009).

43 B. Averboukh, R. Huber, K. W. Cheah, Y. R. Shen, G. G. Qin, Z. C. Ma, and W. H. Zong, J. Appl. Phys. 92, 3564 (2002).

44 L. Khriachtchev, S. Novikov, and J. Lahtinen, J. Appl. Phys. 92, 5856 (2002).

45 S. Godefroo, M. Hayne, M. Jivanescu, A. Stesmans, M. Zacharias, O. I. Lebedev, G. Van Tendeloo, and V. V. Moshchalkov, Nature Nanotech. 3, 174 (2008).

46 F. Iacona, C. Bongiorno, C. Spinella, S. Boninelli, and F. Priolo, J. Appl. Phys. 95, 3723 (2004).

47 F. Iacona, G. Franzo, and C. Spinella, J. Appl. Phys. 87, 1295 (2000).

48 M. Roussel, E. Talbot, P. Pareige, and F. Gourbilleau, J. Appl. Phys. 113, 063519 (2013).

49 B. Garrido, M. Lopez, C. Garcia, A. Perez-Rodriguez, J. R. Morante, C. Bonafos, M. Carrada, and A. Claverie, J. Appl. Phys. 91, 798 (2002).

50 Y. Q. Wang, R. Smirani, and G. G. Ross, J. Cryst. Growth 294, 486 (2006).

51 A. E. Naciri, M. Mansour, L. Johann, J. J. Grob, and C. Eckert, Nucl. Instrum. Meth. B 216, 167 (2004).

52 C. Falcony, W. Calleja, M. Aceves, J. M. Siqueiros, R. Machorro, L. CotaAraiza, G. Soto, and M. H. Farias, J. Electrochem. Soc. 144, 379 (1997).

53 S. Charvet, R. Madelon, F. Gourbilleau, and R. Rizk, J. Lumin. 80, 257 (1998).

54 N. Daldosso, M. Melchiorri, L. Pavesi, G. Pucker, F. Gourbilleau, S. Chausserie, A. Belarouci, X. Portier, and C. Dufour, J. Lumin. 121, 344 (2006).

55 D. Navarro-Urrios, F. Riboli, M. Cazzanelli, A. Chiasera, N. Daldosso, L. Pavesi, C. J. Oton, J. Heitmann, L. X. Yi, R. Scholz, and M. Zacharias, Opt. Mater. 27, 763 (2005).

56 L. Khriachtchev, D. Navarro-Urrios, L. Pavesi, C. J. Oton, N. E. Capuj, and S. Novikov, J. Appl. Phys. 101, 044310 (2007).

57 J. A. Moreno, B. Garrido, P. Pellegrino, C. Garcia, J. Arbiol, J. R. Morante, P. Marie, F. Gourbilleau, and R. Rizk, J. Appl. Phys. 98 (2005).

58 T. P. Chen, Y. Liu, M. S. Tse, S. Fung, and G. Dong, J. Appl. Phys. 95, 8481 (2004).

59 D. Amans, S. Callard, A. Gagnaire, J. Joseph, G. Ledoux, and F. Huisken, J. Appl. Phys. 93, 4173 (2003).

60 S. Mirabella, R. Agosta, G. Franzo, I. Crupi, M. Miritello, R. Lo Savio, M. A. Di Stefano, S. Di Marco, F. Simone, and A. Terrasi, J. Appl. Phys. 106, 103505 (2009).

61 P. Mishra and K. P. Jain, Mat. Sci. Eng. B-Solid 95, 202 (2002).

62 J. von Behren, T. van Buuren, M. Zacharias, E. H. Chimowitz, and P. M. Fauchet, Solid State Commun. 105, 317 (1998).

63 L. Khriachtchev, M. Räsänen, and S. Novikov, Appl. Phys. Lett. 83, 3018 (2003).

64 J. Valenta, T. Ostatnicky, I. Pelant, R. G. Elliman, J. Linnros, and B. Honerlage, J. Appl. Phys. 96, 5222 (2004).

65 I. Pelant, T. Ostatnicky, J. Valenta, K. Luterova, E. Skopalova, T. Mates, and R. G. Elliman, Appl. Phys. B: Lasers Opt. 83, 87 (2006).

66 J. Tauc, Grigorov.R, and A. Vancu, Phys. Status Solidi B 15, 627 (1966).

67 M. BenChorin, B. Averboukh, D. Kovalev, G. Polisski, and F. Koch, Phys. Rev. Lett. 77, 763 (1996).

68 A. Podhorodecki, G. Zatryb, J. Misiewicz, J. Wojcik, and P. Mascher, J. Appl. Phys. 102, 043104 (2007).

69 T. Inokuma, Y. Wakayama, T. Muramoto, R. Aoki, Y. Kurata, and S. Hasegawa, J. Appl. Phys. 83, 2228 (1998).

70 L. Khriachtchev, S. Ossicini, F. Iacona, and F. Gourbilleau, Int. J. Photoenergy 2012, 872576 (2012).

71 N. Daldosso, M. Luppi, S. Ossicini, E. Degoli, R. Magri, G. Dalba, P. Fornasini, R. Grisenti, F. Rocca, L. Pavesi, S. Boninelli, F. Priolo, C. Spinella, and F. Iacona, Phys. Rev. B 68, 085327 (2003).

72 F. Djurabekova and K. Nordlund, Phys. Rev. B 77 (2008).

73 A. Puzder, A. J. Williamson, J. C. Grossman, and G. Galli, J. Am. Chem. Soc. 125, 2786 (2003).

74 M. Luppi and S. Ossicini, J. Appl. Phys. 94, 2130 (2003).

75 I. Vasiliev, J. R. Chelikowsky, and R. M. Martin, Phys. Rev. B 65 (2002).

76 E. Luppi, F. Iori, R. Magri, O. Pulci, S. Ossicini, E. Degoli, and V. Olevano, Phys. Rev. B 75, 033303 (2007).

77 R. Guerra, E. Degoli, and S. Ossicini, Phys. Rev. B 80, 155332 (2009).

78 T. Watanabe, K. Tatsumura, and I. Ohdomari, Appl. Surf. Sci. 237, 125 (2004).

79 R. Guerra, I. Marri, R. Magri, L. Martin-Samos, O. Pulci, E. Degoli, and S. Ossicini, Phys. Rev. B 79, 155320 (2009).

80 R. Guerra and S. Ossicini, Phys. Rev. B 81, 245307 (2010).

81 Z. H. Lu, D. J. Lockwood, and J. M. Baribeau, Nature 378, 258 (1995).

82 S. Dhara, C. Y. Lu, K. G. M. Nair, K. H. Chen, C. P. Chen, Y. F. Huang, C. David, L. C. Chen, and B. Raj, Nanotechnology. 19, 395401 (2008).

83 S. Guha, J. Appl. Phys. 84, 5210 (1998).

84 G. Franzo, M. Miritello, S. Boninelli, R. Lo Savio, M. G. Grimaldi, F. Priolo, F. Iacona, G. Nicotra, C. Spinella, and S. Coffa, J. Appl. Phys. 104, 094306 (2008).

85 M. Roussel, E. Talbot, P. Pareige, and F. Gourbilleau, J. Appl. Phys. 113 (2013).

86 P. F. Trwoga, A. J. Kenyon, and C. W. Pitt, J. Appl. Phys. 83, 3789 (1998).

87 S. Boninelli, F. Iacona, G. Franzo, C. Bongiorno, C. Spinella, and F. Priolo, J. Phys.: Condens. Matter 19, 225003 (2007).

88 L. Khriachtchev, M. Räsänen, S. Novikov, and L. Pavesi, Appl. Phys. Lett. 85, 1511 (2004).

89 L. Khriachtchev, M. Räsänen, S. Novikov, and J. Lahtinen, J. Appl. Phys. 95, 7592 (2004).

90 M. Zacharias, J. Blasing, P. Veit, L. Tsybeskov, K. Hirschman, and P. M. Fauchet, Appl. Phys. Lett. 74, 2614 (1999).

91 M. Zacharias, J. Heitmann, R. Scholz, U. Kahler, M. Schmidt, and J. Blasing, Appl. Phys. Lett. 80, 661 (2002).

92 D. Hiller, M. Jivanescu, A. Stesmans, and M. Zacharias, J. Appl. Phys. 107, 084309 (2010).

93 S. V. Novikov, J. Sinkkonen, O. Kilpela, and S. V. Gastev, J. Cryst. Growth 175, 514 (1997).

94 L. Khriachtchev, M. Räsänen, S. Novikov, O. Kilpela, and J. Sinkkonen, J. Appl. Phys. 86, 5601 (1999).

95 L. Khriachtchev, M. Räsänen, and S. Novikov, Appl. Phys. Lett. 88, 013102 (2006).

96 L. Khriachtchev, S. Novikov, J. Lahtinen, and M. Räsänen, J. Phys.: Condens. Matter 16, 3219 (2004).

97 M. O. Thompson, G. J. Galvin, J. W. Mayer, P. S. Peercy, J. M. Poate, D. C. Jacobson, A. G. Cullis, and N. G. Chew, Phys. Rev. Lett. 52, 2360 (1984).

98 H. Koyama and P. M. Fauchet, J. Appl. Phys. 87, 1788 (2000).

99 L. Khriachtchev, M. Räsänen, and S. Novikov, Appl. Phys. Lett. 86, 141911 (2005).

100 L. Khriachtchev, M. Räsänen, and S. Novikov, J. Appl. Phys. 100, 053502 (2006).

101 L. Khriachtchev and S. Novikov, Appl. Phys. A 87, 761 (2007).

102 H. Koyama and P. M. Fauchet, Appl. Phys. Lett. 73, 3259 (1998).

103 T. Mchedlidze, T. Arguirov, S. Kouteva-Arguirova, and M. Kittler, J. Appl. Phys. 107, 124302 (2010).

104 S. Novikov, J. Sinkkonen, T. Nikitin, L. Khriachtchev, M. Räsänen, and E. Haimi, Microelectron. J. 39, 518 (2008).

105 L. Khriachtchev, Appl. Phys. Lett. 81, 1357 (2002).

106 H. G. Unger, *Planar Optical Waveguides and Fibres* (Clarendon, Oxford, 1977).

107 C. J. Oton, M. Ghulinyan, Z. Gaburro, P. Bettotti, L. Pavesi, L. Pancheri, S. Gialanella, and N. E. Capuj, J. Appl. Phys. 94, 6334 (2003).

108 O. Renault, R. Marlier, M. Gely, B. De Salvo, T. Baron, M. Hansson, and N. T. Barrett, Appl. Phys. Lett. 87, 163119 (2005).

109 S. Kim, M. C. Kim, S. H. Choi, K. J. Kim, H. N. Hwang, and C. C. Hwang, Appl. Phys. Lett. 91, 103113 (2007).

110 E. G. Barbagiovanni, L. V. Goncharova, and P. J. Simpson, Phys. Rev. B 83, 035112 (2011).

111 D. A. G. Bruggeman, Ann. Phys. 416, 636 (1935).

112 M. Balkanski, R. F. Wallis, and E. Haro, Phys. Rev. B 28, 1928 (1983).

113 S. Knief and W. von Niessen, Phys. Rev. B 59, 12940 (1999).

114 A. Hartstein, J. C. Tsang, D. J. Dimaria, and D. W. Dong, Appl. Phys. Lett. 36, 836 (1980).

115 L. Khriachtchev, O. Kilpela, S. Karirinne, J. Keranen, and T. Lepisto, Appl. Phys. Lett. 78, 323 (2001).

116 G. Faraci, S. Gibilisco, P. Russo, A. R. Pennisi, and S. La Rosa, Phys. Rev. B 73, 033307 (2006).

117 I. H. Campbell and P. M. Fauchet, Solid State Commun. 58, 739 (1986).

118 K. Seino, F. Bechstedt, and P. Kroll, Nanotechnology 20 (2009).

119 H. Kogelnik and V. Ramaswamy, Appl. Opt. 13, 1857 (1974).

120 A. Yurtsever, M. Weyland, and D. A. Muller, Appl. Phys. Lett. 89 (2006).

121 G. Zatryb, A. Podhorodecki, J. Misiewicz, J. Cardin, and F. Gourbilleau, Nanoscale Res. Lett. 8 (2013).

122 S. Munekuni, T. Yamanaka, Y. Shimogaichi, R. Tohmon, Y. Ohki, K. Nagasawa, and Y. Hama, J. Appl. Phys. 68, 1212 (1990).

123 Y. D. Glinka, S. H. Lin, L. P. Hwang, and Y. T. Chen, Appl. Phys. Lett. 77, 3968 (2000).

124 E. Borsella, R. D'Amato, F. Fabbri, M. Falconieri, E. Trave, V. Bello, G. Mattei, Y. R. Nie, and D. Y. Wang, Phys. Status Solidi C 8, 974 (2011).

125 L. Koponen, L. O. Tunturivuori, M. J. Puska, and R. M. Nieminen, Phys. Rev. B 79 (2009).

126 C. Garcia, B. Garrido, P. Pellegrino, R. Ferre, J. A. Moreno, L. Pavesi, M. Cazzanelli, and J. R. Morante, Physica E 16, 429 (2003).

127 T. Shimizu-Iwayama, N. Kurumado, D. E. Hole, and P. D. Townsend, J. Appl. Phys. 83, 6018 (1998).

128 K. Kusova, L. Ondic, E. Klimesova, K. Herynkova, I. Pelant, S. Danis, J. Valenta, M. Gallart, M. Ziegler, B. Honerlage, and P. Gilliot, Appl. Phys. Lett. 101 (2012).

129 G. Faraci, S. Gibilisco, and A. R. Pennisi, Phys. Rev. B 80, 193410 (2009).

130 T. Bachels and R. Schafer, Chem. Phys. Lett. 324, 365 (2000).

131 D. V. Murphy and S. R. J. Brueck, Langmuir 8, 494 (1983).

132 R. H. Doremus, J. Appl. Phys. 92, 7619 (2002).

133 K. Wada, A. Suzuki, H. Sato, and R. Kikuchi, J. Phys. Chem. Solids 46, 1195 (1985).

134 K. J. Zhang, M. E. Briggs, R. W. Gammon, and J. V. Sengers, J. Chem. Phys. 104, 6881 (1996).

135 M. Susa and K. Nagata, Mat. Sci. Eng. 146, 51 (1991).

136 B. E. Deal and A. S. Grove, J. App. Phys. 36, 3770 (1965).

137 F. Lukes and E. Schmidt, J. Phys. Chem. Solids 26, 1353 (1965).